The Astrophysical Journal, 920:53 (19pp), 2021 October 10 https://doi.org/10.3847/1538-4357/ac14b8

GRB 180720B: A GRB with Interesting Spectral Characteristics

Jia-Ming Chen[1], Zhao-Yang Peng[1], Tan-Tan Du[1], Yue Yin[2], and Hui Wu[3]
[1] College of Physics and Electronics, Yunnan Normal University, Kunming 650500, People's Republic of China; pengzhaoyang412@163.com
[2] Department of Physics, Liupanshui Normal College, Liupanshui 553004, People's Republic of China
[3] College of information, Yunnan Normal University, Kunming 650500, People's Republic of China
Received 2021 June 6; revised 2021 July 7; accepted 2021 July 13; published 2021 October 12

Abstract

The radiation mechanism and jet composition of gamma-ray bursts (GRBs) are still two important unresolved issues, and studying its energy spectrum characteristics can provide us with evidence. In this paper, we first use the smoothly broken power-law function (Band) and the cutoff power-law function to perform Bayesian time-resolved spectrum analysis on GRB 180720B and find these spectra can be fitted well. When the thermal component is added, approximately 40% of the resolution spectrum fitting statistics are significantly improved, indicating that there is a thermal spectral component in the burst. The thermal spectra are concentrated at the beginning and peak stage of the pulses. Therefore, the burst also supports that the GRB jet component transitions from material dominance to magnetic dominance. The values of the low-energy spectrum index α of the time-resolved spectra do not exceed the so-called synchrotron line of death, regardless of whether the thermal components are added or not, which indicates that the burst can be explained by synchrotron radiation. Moreover, we find that both α and E_p track the flux, but their tracking modes are different. We use the synchrotron model to fit these time-resolved spectra and find that these spectra can also be well fitted by the model. Furthermore, we find that both the electron spectrum index p and the magnetic field strength B track the flux and are positively correlated with the flux. Our results also show that the Band function can be explained by the synchrotron model in the Gamma-ray Burst Monitor energy range.

Unified Astronomy Thesaurus concepts: Gamma-ray bursts (629)

1. Introduction

Gamma-ray bursts (GRBs) are currently the most violent explosion phenomenon in the universe. According to their duration, they can be divided into long GRBs (LGRBs) and short GRBs (SGRBs), and the dividing line is about 2 s. Researchers generally believe that LGRBs come from black holes or magnetars after the death of massive stars, while the origin of SGRBs is the merger of dense binary stars (Narayan et al. 1992; Woosley 1993; MacFadyen & Woosley 1999; Woosley & Bloom 2006; Kumar & Zhang 2015). Various observations and studies have been carried out over 50 yr after the discovery of the GRB, but there are still many unresolved problems in the prompt emission phase (Zhang 2011; Kumar & Zhang 2015): (1) What is the composition of the GRB jet (baryon fireball or Poynting flux)? (2) What is the energy dissipation mechanism (from shock waves or magnetic reconnection) that GRB jets convert other forms of energy into radiation? (3) What is the particle acceleration mechanism of GRB prompt emission? (4) What is the radiation mechanism of GRB prompt emission (synchrotron radiation, synchrotron self-Compton radiation, or Comptonization of quasi-thermal radiation from the photosphere)? Spectral analysis is a key clue to help us answer these questions.

An important theory that has been put forward in the literature is that the GRB jet may originate from a hot fireball. However, our observation results showed that in its prompt emission phase, most of the GRB spectra can be fitted by the nonthermal Band function (Band et al. 1993; Briggs et al. 1999; Abdo et al. 2009; Yu et al. 2016; Zhang et al. 2016). Based on the model, the fireball is dominated by baryons and the prompt emission may come from internal shock waves or fireball photospheres (Meszaros & Rees 1993; Mészáros & Rees 2000; Rees & Mészáros 2005), which causes the observed spectrum to be a superposition of the nonthermal component from the shock wave in the optically thin and the quasi-thermal component from the fireball photosphere. Another possible model of the GRB jet is the Poynting-flux-dominated outflow from the engine (Daigne & Mochkovitch 2002; Zhang & Pe'er 2009). The Poynting-flux-dominated jet is different from that of the fireball, in which the thermal component is negligible. In the jet where Poynting flux is dominant, most of the energy is contained in the Poynting flux. Most GRB prompt emission energy is converted from the original form of Poynting flux energy (Granot et al. 2011). In fact, the jet composition of different GRBs may be different. Most likely, the jet components may be mixed (Gao & Zhang 2015; Li 2019a, 2020), which is characterized by relativistic outflow, with hot fireball components and cold Poynting flux components.

Photospheric radiation and synchrotron radiation are widely present in GRB spectra, indicating that the jet compositions are different (Li 2019a). Observations show that the energy spectrum components of GRB seem to be diverse, and some GRBs do show the characteristic properties of fireballs with thermal components (Abdo et al. 2009; Ryde et al. 2010; Pe'Er et al. 2012). Others show evidence of Poynting-flux dominance (Metzger et al. 2011; Lei et al. 2013). Moreover, analysis of Fermi spectroscopy shows that thermal components present different time and spectral characteristics: some thermal components can be detected during the entire duration of prompt emission (Ryde 2004; Ghirlanda et al. 2013); some can only be found at the beginning of the burst and followed by nonthermal components (Zhang et al. 2018; Li 2019a).

Spectral characteristics are the key to understanding the physical origin of GRBs, such as the energy dissipation mechanism, radiation mechanism, jet structure, and the characteristics of the central engine. Some of the observed energy/luminosity-spectral relationships involving E_p are extensively discussed in the literature. The peak energy E_p is one of the most interesting parameter evolutions of GRBs. It has evolved drastically over time. During the Burst and Transient Source Experiment (BATSE) period, E_p showed several different patterns: (1) the trend of hard to soft, regardless of the rise and fall of flux, is monotonically decreasing (Norris et al. 1986; Bhat et al. 1994; Kaneko et al. 2006); (2) the flux tracking trend, that is, follows the rise and fall of flux (Golenetskii et al. 1983; Briggs et al. 1999; Lu et al. 2010; Peng et al. 2010; Hakkila & Preece 2011); (3) soft-to-hard trend or chaotic evolution (Laros et al. 1985; Kargatis et al. 1994).

After the launch of Fermi in 2008, with the improvement of the quality of spectral data, it was confirmed that the first two modes were dominant: hard to soft accounted for about two-thirds, and flux tracking accounted for about one-third (Yu et al. 2018; Li 2019b). The physical origin of these evolutionary patterns is still unresolved, although some solutions have been proposed in the literature (Lu et al. 2010; Oganesyan et al. 2018, 2019; Uhm et al. 2018). Compared with the E_p evolution, the α evolution is more chaotic, so there are relatively few studies and physical explanations. Li et al. (2019) found that the E_p and α evolutions of GRB 131231A both exhibit flux tracking behavior, and are defined as the double tracking mode of spectral evolution.

GRB 180720B, a GRB observed by Fermi (co-detected by the Gamma-ray Burst Monitor (GBM) and the Large Area Telescope (LAT)) and Swift (co-detected by the Burst Alert Telescope (BAT) and X-Ray Telescope (XRT)) is a long-term, extremely bright multi-pulse GRB. It provides a good example for us to study the spectral evolution and radiation mechanism of GRBs. In this work, we perform detailed time-resolved spectrum analysis of GRB 180720 using Bayesian methods. In Section 2, we introduce the sample selection and analysis methods; in Section 3, the spectral models used in this article are described; in Section 4, the spectral analysis results are given, including the evolution of the spectrum, the distribution of parameters, and the inter-parameter relationship. We present the discussion and summarizes in Section 5.

2. Data and Analysis Methods

The Fermi GRB Detector (GBM) consists of 14 detectors (Meegan et al. 2009), 12 of which are sodium iodide (NaI, named n0–n9, na, and nb) detectors with a coverage area of approximately 8 keV–1 MeV and two are non-directional, two bismuth germanate (BGO, called b0 and b1) detectors with a coverage range of approximately 200 keV–40 MeV. This arrangement makes Fermi/GBM a powerful detector with an energy range of more than 3 orders of magnitude.

On 2018 July 20, UT 14:21:39.65, Fermi/GBM triggered and located the bright GRB 180720B; 5 s later, 14:21:44 UT, BAT triggers and locates the same event (Siegel et al. 2018). The Swift XRT detected its bright afterglow within less than 90 s, and then lasted for more than 30 days, making it the brightest XRT GRB after the abnormal GRB 130427A, in the 0.3−10 keV energy range. In addition, a redshift of Z = 0.653 was obtained (Vreeswijk et al. 2018) based on the multiple follow-up observations with optical telescopes.

The preliminary GRB data will be uploaded to the NASA/HEASARC database within a few minutes after the trigger, including the trigger file and the light curve for quick viewing. Detailed data files with the highest time resolution (CTIME and TTE files) and spectral resolution (CSPEC and TTE files) can be downloaded from the spacecraft within a few hours. This makes the online Fermi/GBM GRB database the latest GRB data repository.[4] Compared with CSPEC files, TTE files have the smallest time resolution (2μ) and the best energy resolution, so they are suitable for analyzing time-resolved spectrum of GRB. The use of TTE data and standard response files is provided by the GBM team. We select data from all NaI detectors triggered by GBM (0−3 in most cases) and the brightest BGO detector. Figure 1 shows the light-curve and spectrum analysis range of the detector selected.

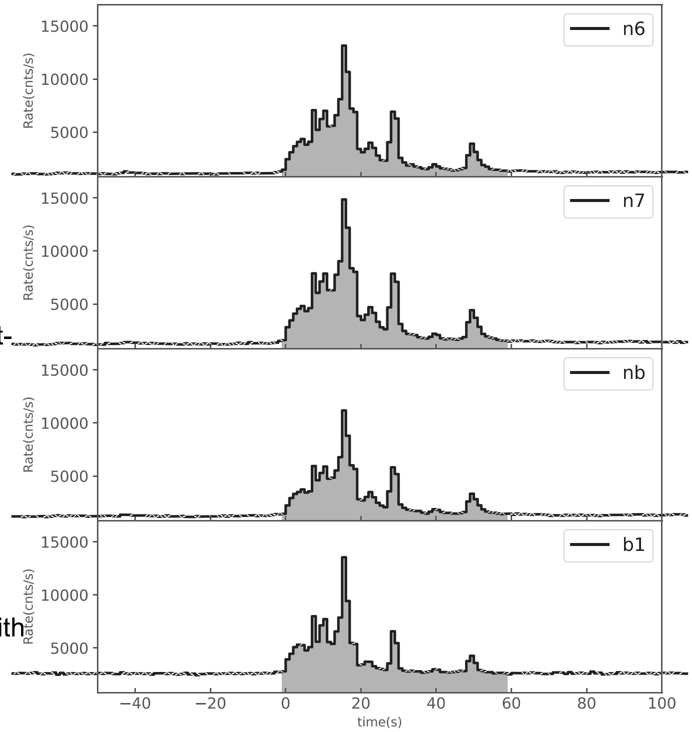

Figure 1. Range of the GRB 180720B light-curve and energy spectrum analysis. The black line and gray shading indicate the range of the light-curve and energy spectrum analysis, respectively (0 ~ 55 s). We used the TTE type of GBM data included NaI detectors 6, 7, nb, and BGO detector 1.

In order to track and study the spectral evolution in the burst, detailed time-resolved spectral information is required. In this paper, we use the Multi-Mission Maximum Likelihood Framework 3ML (Vianello et al. 2015) software package as the main tool for time-resolved spectral analysis of Fermi/GBM data (Yu et al. 2018). For a detailed analysis of the process of 3ML data, please refer to Li (2019a). Traditional spectral analysis methods usually use the signal-to-noise ratio method to slice time. This method can ensure that there are enough photons to perform spectral analysis, but it may destroy the physical structure. Burgess (2014) compared four time-slicing methods. He concluded that to obtain the most delicate time slicing while minimizing the influence of the mixed spectrum caused by the inherent spectral evolution, the Bayesian Blocks method should be used. BBlock has the following characteristics: (1) Each bin obtained has a constant Poisson rate. (2) Each bin has a different width and signal-to-

[4] The data can be obtained by either visiting https://heasarc.gsfc.nasa.gov/W3Browse/fermi/fermigbrst.html.

noise ratio. (3) The algorithm is used to subdivide the GRB light-curve flux for time bin selection. (4) The selection of time bin reflects the true variability of the data. However, the BBlock method cannot guarantee enough photons in each bin to perform accurate spectral fitting. Therefore, to ensure that there are enough photons to perform spectral fitting without destroying the physical structure. We first apply the BBlock method with alarm probability p = 0.01 (Scargle et al. 2013) to the TTE light curve of one of the brightest NaI detectors, and the other detectors follow the same time bin information. Then we calculate the statistical significance S (an appropriate measure of signal-to-noise ratio) for each bin and select bins with S > 20 (Vianello 2018).

3. Spectral Model

The empirical model is usually used in the energy spectrum analysis of GRBs. We first want to use empirical functions to fit the time-resolved spectra of GRBs, and then we want to check whether there are thermal components in these time-resolved spectra, and finally we want to see whether these spectra can also be fitted by physical models.

We first use the most widely used smoothing inflection power-law function (Band) and cutoff power-law function (CPL) (Band et al. 1993; Gruber et al. 2014). The Band function empirical model is

$$f_{\rm Band}(E) = A\begin{cases}\left(\frac{E}{100\,{\rm keV}}\right)^{\alpha}\exp\left[-\frac{(\alpha+2)E}{E_p}\right], & E < E_c,\\ \left(\frac{E}{100\,{\rm keV}}\right)^{\beta}\exp(\beta-\alpha)\left(\frac{E_c}{100\,{\rm keV}}\right)^{\alpha-\beta}, & E \geq E_c,\end{cases} \quad (1)$$

where A is the normalization constant of spectral fitting, the unit is photons cm^{-2} keV^{-1} s^{-1}; E_p is the peak energy of the energy spectrum, in kiloelectronvolts; α and β are the low-energy and high-energy power-law spectral indices, respectively.

The CPL function empirical model is

$$f_{\rm CPL}(E) = A\left(\frac{E}{100\ {\rm keV}}\right)^{\alpha}\exp\left[-\frac{(\alpha+2)E}{E_p}\right], \quad (2)$$

where A is the normalization factor unit when 100 keV is photons cm^{-2} keV^{-1} s^{-1}; E_p is the peak energy, and α is the low-energy power-law photon spectral index.

Some bursts have additional thermal components, and are generally fitted with the Planck blackbody (BB) function,

$$f_{\rm BB}(E) = A(t)\frac{E^2}{\exp[E/kT]-1}, \quad (3)$$

where A is the normalization, k is the Boltzmann constant, and kT is the BB temperature.

The transformation from traditional empirical fitting functions to physical models is a natural first choice, which will provide a more reliable test for characterizing the GRB environment. In this article, the physical model we use is a parametric synchrotron model, which Burgess et al. (2020) has packaged as a Python package. The cool synchrotron model is as follows:

$$n_\gamma(\epsilon; K, B, p, \gamma_{\rm cool}) = \int_0^{t'(\gamma_{\rm cool})}\int_1^{\gamma_{\max}} dt\, d\gamma'\, n_e(\gamma, t)\,\Phi\left(\frac{\epsilon}{\epsilon_{\rm crit}(\gamma, B)}\right), \quad (4)$$

where K is the arbitrary normalization constant of flux, B is the magnetic field strength (unit: Gauss), p is the electron injection index, and $\gamma_{\rm cool}$ is the energy of electron cooling during the synchrotron cooling time, unit: kiloelectronvolts.

$$\Phi(w) = \int_w^{\infty} dx\, K_{5/3}(x), \quad (5)$$

where $K_{5/3}$ is a Bessel function, $B_{\rm crit} = 4.13 \times 10^{13}$ G, n_e is determined by solving the electron cooling equation using the Chang and Cooper method. Under synchrotron radiation cooling, the evolution of the electron distribution function obeys the Fokker–Planck equation:

$$\frac{\partial n_e(\gamma, t)}{\partial t} = \frac{\partial}{\partial\gamma}C(\gamma)n_e(\gamma, t) + Q(\gamma). \quad (6)$$

Suppose electrons are continuously injected between Lorentz factors $\gamma_{\min}$ and $\gamma_{\rm cool}$ with a constant exponent p, so that

$$Q(\gamma) \propto \gamma^{-p}; \quad \gamma_{\rm inj} \leq \gamma \leq \gamma_{\max}, \quad (7)$$

and cooled via emission of synchrotron photons:

$$C(\gamma) = -\frac{\sigma_T B^2}{6\pi m_e c}\gamma^2, \quad (8)$$

where σ_T is the Thomson cross section, m_e is the mass of the electron, and c is the speed of light.

The model has five parameters: B, $\gamma_{\rm cool}$, $\gamma_{\rm inj}$, $\gamma_{\max}$, and p. There is a strong degeneracy between B and $\gamma_{\rm inj}$, so we choose to fix $\gamma_{\rm inj} = 10^5$. In addition, the fast cooling synchrotron model fits the spectrum very poorly (Burgess et al. 2014). Therefore, we set the ratio of $\gamma_{\rm cool}$ and $\gamma_{\rm inj}$ in the slow cooling range and fix $\gamma_{\max} = 10^8$.

Previous studies have shown that GRB spectra may contain three basic components (Zhang et al. 2011): (i) nonthermal components, which can usually be fitted by the synchrotron radiation model, the Band function, and the CPL function (wider spectrum); (ii) can be fitted by Planck function (BB) (narrower spectral peak) or thermal component; the observed GRB spectrum can be a combination of two of these components, or a combination of all components in a GRB at the same time (Gao & Zhang 2015). The multi-spectral component analysis of Fermi GRB shows that although most of it is nonthermal radiation, a single band function cannot fully explain all GRB spectra (Guiriec et al. 2013). In addition, if the BB component is added to the nonthermal Band function, in many cases, the quality of the fitting will be significantly improved, which better describes the spectrum of these GRBs, indicating that a small part of the radiation energy obviously comes from the BB component. Adding the BB component to the spectrum allows quantitative analysis of its properties to determine its source (Ryde et al. 2010; Pe'Er et al. 2012). The Li (2019a) analysis shows that the BB component is very important, and it will seriously affect the spectral parameters and the corresponding physical interpretation. Therefore, we need to introduce the BB component to conduct a comprehensive analysis of GRB 180720B.

In order to check whether there is a thermal component in the spectrum, we first fit the data using models such as Band and CPL; then, an additional BB component is added to check whether it improves the fitting statistics. In order to select the best model from two different given models, we adopt the deviation information criterion (DIC), defined as, $\mathrm{DIC} = -2\log[p(\mathrm{data}|\hat{\theta})] + 2p_{\mathrm{DIC}}$, where $\hat{\theta}$ is the posterior mean of the model, and p_{DIC} is the effective number of parameters. The best model is the model with the lowest DIC; we define

$$\Delta\mathrm{DIC}_{\mathrm{CPL}} = \mathrm{DIC}_{\mathrm{CPL+BB}} - \mathrm{DIC}_{\mathrm{CPL}},$$
$$\Delta\mathrm{DIC}_{\mathrm{Band}} = \mathrm{DIC}_{\mathrm{Band+BB}} - \mathrm{DIC}_{\mathrm{Band}}. \quad (9)$$

If the BB component is introduced, the $\Delta\mathrm{DIC} < -10$ in the sample (CPL + BB fitting is better than CPL fitting alone), indicating that there is a BB (thermal) component in the spectrum (Yu et al. 2018; Li 2019a).

4. Results of the Analysis

We first use two empirical models to fit the time-resolved spectra, and then we refit them after adding thermal components separately. Tables 1 and 2 list the fitting results of the CPL and Band models alone and after adding thermal components, respectively. Then we use the slow cooling synchrotron model to refit these spectra. Table 3 lists the parameters of the fitting of the synchrotron model (electron injection index p, magnetic field strength B (G), electron cooling energy γ_{cool} (kiloelectronvolts), and energy flux F (erg cm^{-2} s^{-1})).

4.1. Distribution of Parameters

Figures 2 and 3 show the parameter distributions of CPL, Band, and synchrotron models, including α, β, p, B, γ_{cool}, energy flux F, and E_p. Table 4 lists the means and standard deviations of the distributions. Since the error of fitting spectral parameters cannot be taken into account in the histogram, we performed a kernel density estimation (KDE) for the distribution of each parameter.

As shown in Figures 2 and 3, and Table 4, the average values of CPL and Band low-energy photon index α distribution are −1.09 ± 0.17 and −1.03 ± 0.17, which is basically the same as the typical value α ~ − 1 (Preece et al. 2000). We also find that all of the low-energy index α do not exceed the so-called synchrotron dead line (− 3/2 < α < − 2/3). The distribution of the low-energy spectral index α of the CPL model shows a bimodal structure trend, and the two peaks are at ~ −1 and ~ −1.4. The distribution of the low-energy spectral index α of the Band model is similar to that of CPL, with a peak at ~ −0.8, and a small peak at ~ −1.4. The average value of β is −2.43 ± 0.27, and the peak value is between −2.50 and −2.25. Figure 4 shows the mean value of p, B, and γ_{cool} are 3.03 ± 0.41, 587.08 ± 456.52 (G), and 4.44 ± 2.24) × 10^6 keV, respectively. We can also find that the distributions of p and γ_{cool} seem to show single peak profile, while B appears to be two peaks.

4.2. Thermal Composition Analysis

To check the thermal component in the energy spectrum, we first use the empirical model to fit separately, then add the BB component to fit, and check the difference ΔDIC of the statistic (DIC). If $\Delta\mathrm{DIC} < -10$, it means that the spectrum contains significant thermal components. Figure 5 shows the evolution and distribution of the ΔDIC of the best model.

It can be seen from the figure that whether it is the Band model or the CPL model plus the BB component, the DIC of the fitting statistics has been improved. The number of spectra with the DIC of the best model less than −10 accounted for 35% (26/73). For the spectrum fitted by the CPL model, $\Delta\mathrm{DIC}_{\mathrm{CPL}}$ is less than zero in the analysis of the pulse range, indicating a thermal component that improves the result of the entire spectrum fitting. This result is consistent with the results of the analysis of Moradi et al. (2021). They used CPL and CPL+BB models to analyze 15 ~ 18 s pulses. The ΔDIC obtained was less than −10, indicating that the BB model improved the fitting results. In the pulse range of our analysis, $\Delta\mathrm{DIC}_{\mathrm{CPL}}$ is less than 0, but $\Delta\mathrm{DIC}_{\mathrm{Band}}$ appears to be greater than 0 at the end of the pulse. The reason may be that there are fewer high-energy photons in the late pulse, and the Band model does not limit the spectrum well. The spectrum of $\Delta\mathrm{DIC} < -10$ is mainly distributed in the early period of the pulse, indicating that the thermal component primarily exists in the early period of the pulse and gradually decreases with time.

4.3. Parameter Evolution

The evolution of α, E_p, p, and B with time is shown in Figures 6 and 7, where α and E_p are from the best model parameters. Spectral parameters have a hard-to soft mode, that is, the decrease of the parameter has nothing to do with the rise and decay of the pulse, and the parameters also show a flux tracking mode, the parameter is related to the rise and fall of flux. Recently, Yu et al. (2018) and Li (2019b) reported findings that showed the E_p–flux tracking trend. Li et al. (2019) performed detailed time-resolved spectral fitting of the single-pulse GRB 131231A and found that both the low-energy spectrum index α and the peak energy E_p has the flux tracking mode (double tracking). GRB 180720B is a more complex multi-pulse GRB, and the evolution of its low-energy spectrum index α and peak energy E_p is very fascinating. Figure 6 shows that the spectral index α demonstrates a powerful flux tracking mode, and the electronic spectrum index p of the synchrotron model also has this mode. Figure 7 shows the evolution of E_p. It can be seen that E_p first follows a hard-to-soft mode, then shows a flux tracking mode, which is different from the evolution mode of α; and B always shows a very strong flux tracking mode. Figure 8 shows the comparison of the evolutionary modes of E_p–α and B–p, where E_p–α shows the opposite evolution in the initial stage, but it later offers a double tracking model. While B–p show a double tracking model throughout the analysis stage. The spectral parameters of the multi-pulse GRB 180720B show strong flux tracking behavior, and we guess that the parameters showed a strong monotonic positive correlation. A detailed parameter correlation analysis will be given below.

4.4. Correlations between Spectral Parameters

Correlation analysis plays an essential role in understanding GRB physics because it provides clues to help us reveal their nature. Figures 9–11 show the parameter relationships between the three models (including the model after introducing the thermal component), namely, $\log(F)-\alpha$, $\log(E_p)-\log(F)$,

Table 1
Results of the Time-resolved Spectrum Analysis of GRB 180720B Fit by the CPL model

t_{start}~ t_{stop}	S	CPL			CPL plus BB			
		α	E_p (keV)	F (× 10^{-6} erg^{-1} cm^{-2} s^{-1})	α	E_p (keV)	kT (keV)	F (× 10^{-6} erg^{-1} cm^{-2} s^{-1})
(1)	(2)	(3)	(4)	(5)	(6)	(7)	(8)	(9)
1.01–1.58	23.31	$-1.15^{+0.04}_{-0.04}$	$3578.47^{+2351.24}_{-2374.16}$	$8.69^{+2.14}_{-1.92}$	$-1.14^{+0.04}_{-0.04}$	$3555.63^{+2095.03}_{-2230.32}$	$3.78^{+1.98}_{-2.25}$	$8.74^{+2.46}_{-2.05}$
1.58–2.90	54.86	$-1.08^{+0.02}_{-0.02}$	$2313.42^{+618.31}_{-617.48}$	$13.78^{+1.64}_{-1.54}$	$-1.07^{+0.02}_{-0.02}$	$2304.90^{+586.18}_{-603.41}$	$3.58^{+3.10}_{-2.29}$	$13.87^{+1.74}_{-1.65}$
2.90–4.08	67.51	$-1.00^{+0.02}_{-0.02}$	$1786.65^{+382.73}_{-386.83}$	$17.44^{+2.02}_{-2.14}$	$-0.99^{+0.02}_{-0.02}$	$1780.76^{+375.33}_{-379.95}$	$3.01^{+1.48}_{-1.78}$	$17.46^{+2.37}_{-1.94}$
4.08–6.47	110.12	$-0.94^{+0.02}_{-0.02}$	$948.68^{+12.09}_{-115.28}$	$12.90^{+1.13}_{-0.97}$	$-0.91^{+0.02}_{-0.02}$	$1095.24^{+178.12}_{-173.21}$	$20.59^{+1.62}_{-1.64}$	$13.86^{+1.64}_{-1.32}$
6.47–7.64	66.75	$-1.03^{+0.03}_{-0.03}$	$806.66^{+231.54}_{-233.21}$	$8.30^{+1.39}_{-1.06}$	$-1.03^{+0.03}_{-0.03}$	$875.73^{+363.00}_{-338.74}$	$8.71^{+9.92}_{-7.25}$	$8.89^{+3.05}_{-1.77}$
7.64–7.99	53.22	$-1.02^{+0.03}_{-0.03}$	$1838.02^{+647.64}_{-656.37}$	$26.33^{+5.20}_{-4.54}$	$-1.01^{+0.03}_{-0.03}$	$1899.18^{+712.77}_{-697.81}$	$7.58^{+13.41}_{-6.23}$	$27.37^{+6.49}_{-5.58}$
7.99–8.40	73.51	$-1.00^{+0.02}_{-0.02}$	$2007.95^{+397.86}_{-390.05}$	$40.32^{+4.46}_{-4.02}$	$-1.00^{+0.02}_{-0.02}$	$2003.68^{+399.41}_{-393.76}$	$2.87^{+1.38}_{-1.61}$	$40.29^{+4.65}_{-4.30}$
8.40–8.73	80.46	$-0.86^{+0.03}_{-0.03}$	$875.38^{+161.38}_{-159.33}$	$29.26^{+4.33}_{-3.69}$	$-0.94^{+0.03}_{-0.03}$	$1531.08^{+425.14}_{-416.54}$	$34.54^{+2.19}_{-1.89}$	$38.29^{+6.52}_{-6.03}$
8.73–9.33	87.60	$-1.02^{+0.02}_{-0.02}$	$760.77^{+152.20}_{-157.02}$	$16.68^{+2.05}_{-1.57}$	$-1.01^{+0.03}_{-0.03}$	$755.70^{+169.63}_{-160.00}$	$4.86^{+4.41}_{-3.49}$	$16.96^{+2.28}_{-2.11}$
9.33–10.34	89.19	$-1.00^{+0.02}_{-0.02}$	$601.37^{+99.95}_{-102.46}$	$10.93^{+1.19}_{-0.94}$	$-1.00^{+0.03}_{-0.03}$	$668.14^{+201.75}_{-192.71}$	$16.60^{+4.95}_{-4.03}$	$11.77^{+2.64}_{-1.83}$
10.34–11.02	101.89	$-0.93^{+0.02}_{-0.02}$	$1039.06^{+148.85}_{-147.02}$	$27.08^{+2.43}_{-2.19}$	$-0.92^{+0.02}_{-0.02}$	$1037.75^{+151.61}_{-146.17}$	$6.69^{+6.76}_{-5.23}$	$27.39^{+3.41}_{-2.60}$
11.02–11.27	54.80	$-0.98^{+0.04}_{-0.04}$	$763.85^{+217.32}_{-232.01}$	$17.04^{+3.48}_{-2.62}$	$-0.94^{+0.05}_{-0.05}$	$819.45^{+257.20}_{-264.62}$	$13.23^{+6.69}_{-10.61}$	$17.88^{+5.42}_{-3.45}$
11.27–12.33	129.40	$-0.95^{+0.02}_{-0.02}$	$978.75^{+140.42}_{-131.56}$	$26.59^{+2.34}_{-2.05}$	$-0.97^{+0.02}_{-0.02}$	$1304.61^{+252.37}_{-242.12}$	$26.57^{+1.90}_{-1.91}$	$30.66^{+3.79}_{-3.12}$
12.33–12.64	59.43	$-1.00^{+0.04}_{-0.04}$	$473.83^{+120.54}_{-122.29}$	$10.56^{+1.61}_{-1.43}$	$-0.99^{+0.06}_{-0.07}$	$556.18^{+242.95}_{-241.22}$	$13.85^{+8.01}_{-10.86}$	$11.22^{+4.67}_{-2.44}$
12.64–13.33	61.19	$-1.13^{+0.03}_{-0.03}$	$443.35^{+131.57}_{-131.97}$	$6.25^{+0.90}_{-0.79}$	$-1.12^{+0.04}_{-0.04}$	$456.54^{+143.08}_{-145.88}$	$6.73^{+6.21}_{-5.20}$	$6.41^{+1.52}_{-0.82}$
13.33–13.50	39.65	$-0.94^{+0.05}_{-0.06}$	$395.30^{+104.42}_{-113.23}$	$8.70^{+1.86}_{-1.47}$	$-0.93^{+0.06}_{-0.06}$	$392.96^{+115.2}_{-108.58}$	$3.84^{+2.70}_{-2.47}$	$8.86^{+2.06}_{-1.55}$
13.50–14.19	95.12	$-0.92^{+0.02}_{-0.02}$	$490.96^{+63.16}_{-64.72}$	$13.88^{+1.21}_{-1.22}$	$-0.93^{+0.05}_{-0.05}$	$612.95^{+154.91}_{-159.57}$	$20.98^{+3.45}_{-3.58}$	$15.03^{+2.97}_{-2.19}$
14.19–14.41	64.62	$-1.00^{+0.03}_{-0.03}$	$750.74^{+204.85}_{-200.73}$	$20.95^{+3.77}_{-2.86}$	$-0.95^{+0.06}_{-0.06}$	$796.52^{+238.66}_{-225.24}$	$13.94^{+4.47}_{-3.21}$	$21.92^{+5.27}_{-3.93}$
14.41–14.79	65.23	$-1.06^{+0.04}_{-0.04}$	$451.45^{+124.55}_{-126.26}$	$9.87^{+1.59}_{-1.26}$	$-1.03^{+0.06}_{-0.06}$	$614.69^{+259.89}_{-265.70}$	$15.74^{+2.14}_{-2.14}$	$11.09^{+3.17}_{-2.27}$
14.79–15.05	73.87	$-0.90^{+0.03}_{-0.03}$	$709.22^{+122.56}_{-122.14}$	$24.78^{+3.20}_{-2.80}$	$-0.90^{+0.03}_{-0.03}$	$784.35^{+208.45}_{-201.97}$	$16.75^{+10.29}_{-14.64}$	$26.42^{+8.31}_{-4.52}$
15.05–15.50		$-1.01^{+0.03}_{-0.03}$	$440.50^{+84.90}_{-86.95}$	$11.24^{+1.37}_{-1.21}$	$-1.01^{+0.06}_{-0.06}$	$530.54^{+191.61}_{-188.05}$	$16.91^{+4.69}_{-4.12}$	$12.30^{+3.19}_{-2.35}$
15.50–15.84	88.96	$-0.90^{+0.02}_{-0.02}$	$820.95^{+144.07}_{-149.76}$	$30.31^{+3.90}_{-3.36}$	$-0.96^{+0.04}_{-0.04}$	$1379.27^{+438.29}_{-466.41}$	$29.23^{+3.50}_{-3.51}$	$39.20^{+8.72}_{-7.22}$
15.84–16.29	129.66	$-0.90^{+0.02}_{-0.02}$	$1018.79^{+150.47}_{-151.25}$	$50.68^{+4.90}_{-5.01}$	$-0.97^{+0.02}_{-0.02}$	$1620.52^{+293.71}_{-294.97}$	$35.88^{+2.15}_{-2.26}$	$62.65^{+7.25}_{-6.39}$
16.29–16.44	91.86	$-0.89^{+0.03}_{-0.03}$	$1022.31^{+211.15}_{-203.59}$	$70.81^{+11.23}_{-9.17}$	$-1.00^{+0.02}_{-0.02}$	$1774.46^{+400.68}_{-402.08}$	$44.85^{+2.35}_{-2.38}$	$86.46^{+12.08}_{-9.36}$
16.44–16.63	115.87	$-0.93^{+0.01}_{-0.02}$	$1667.23^{+215.53}_{-211.83}$	$116.07^{+10.78}_{-9.51}$	$-0.97^{+0.02}_{-0.02}$	$2327.89^{+437.25}_{-432.23}$	$43.71^{+2.56}_{-2.73}$	$129.77^{+14.23}_{-13.26}$
16.63–16.72	67.36	$-0.95^{+0.04}_{-0.04}$	$942.71^{+298.39}_{-290.85}$	$53.35^{+10.77}_{-9.36}$	$-1.06^{+0.04}_{-0.04}$	$1709.15^{+716.42}_{-751.87}$	$40.15^{+3.91}_{-3.50}$	$67.17^{+15.72}_{-13.44}$
16.72–16.88	73.76	$-0.93^{+0.03}_{-0.03}$	$642.91^{+121.41}_{-123.15}$	$31.48^{+4.02}_{-3.96}$	$-0.87^{+0.06}_{-0.06}$	$667.11^{+148.33}_{-152.65}$	$13.00^{+3.52}_{-2.59}$	$32.71^{+6.92}_{-5.45}$
16.88–17.31	99.02	$-1.03^{+0.02}_{-0.02}$	$443.80^{+68.92}_{-72.00}$	$16.32^{+1.57}_{-1.38}$	$-1.03^{+0.05}_{-0.05}$	$519.91^{+153.32}_{-158.97}$	$17.58^{+5.00}_{-4.68}$	$17.25^{+4.05}_{-2.51}$
17.31–17.43	72.22	$-0.90^{+0.03}_{-0.03}$	$739.31^{+135.23}_{-127.66}$	$41.16^{+5.33}_{-4.67}$	$-0.86^{+0.05}_{-0.04}$	$796.50^{+156.26}_{-159.19}$	$17.71^{+4.79}_{-3.46}$	$42.83^{+8.05}_{-6.42}$
17.43–17.49	60.24	$-0.76^{+0.04}_{-0.04}$	$766.02^{+157.63}_{-149.17}$	$64.32^{+14.81}_{-10.12}$	$-0.76^{+0.06}_{-0.05}$	$848.62^{+220.82}_{-251.43}$	$15.99^{+14.75}_{-14.08}$	$68.14^{+32.20}_{-14.96}$
17.49–17.72	105.16	$-0.87^{+0.02}_{-0.02}$	$664.22^{+81.13}_{-80.63}$	$42.93^{+3.91}_{-3.36}$	$-0.86^{+0.02}_{-0.03}$	$669.78^{+83.27}_{-81.04}$	$8.59^{+8.57}_{-7.05}$	$44.07^{+5.34}_{-4.07}$
17.72–17.99	81.61	$-1.02^{+0.03}_{-0.03}$	$434.23^{+79.17}_{-79.95}$	$17.49^{+1.93}_{-1.65}$	$-1.06^{+0.05}_{-0.05}$	$516^{+217.61}_{-211.75}$	$19.35^{+7.80}_{-11.86}$	$1904^{+6.33}_{-3.92}$
17.99–18.61	102.32	$-1.06^{+0.03}_{-0.03}$	$381.21^{+65.03}_{-60.69}$	$11.72^{+1.07}_{-0.92}$	$-1.05^{+0.03}_{-0.03}$	$399.85^{+77.52}_{-79.88}$	$10.68^{+5.23}_{-8.18}$	$12.02^{+1.76}_{-1.20}$
18.61–18.67	43.71	$-0.84^{+0.07}_{-0.07}$	$233.06^{+50.90}_{-51.13}$	$12.98^{+2.84}_{-2.32}$	$-0.84^{+0.07}_{-0.07}$	$234.54^{+52.72}_{-53.01}$	$5.49^{+5.59}_{-3.99}$	$13.16^{+3.51}_{-2.32}$
18.67–19.11	81.64	$-1.13^{+0.03}_{-0.03}$	$255.39^{+52.22}_{-52.76}$	$8.51^{+0.85}_{-0.77}$	$-1.13^{+0.04}_{-0.04}$	$265.24^{+64.41}_{-69.68}$	$7.64^{+6.14}_{-5.91}$	$8.63^{+1.50}_{-1.04}$
19.11–19.38	89.75	$-1.04^{+0.03}_{-0.03}$	$509.71^{+92.23}_{-89.95}$	$21.46^{+2.30}_{-1.90}$	$-1.04^{+0.04}_{-0.04}$	$582.63^{+171.36}_{-171.31}$	$17.39^{+5.83}_{-4.52}$	$23.15^{+4.44}_{-3.43}$
19.38–19.50	50.49	$-1.07^{+0.06}_{-0.06}$	$256.72^{+78.42}_{-79.37}$	$9.85^{+2.01}_{-1.42}$	$-1.09^{+0.08}_{-0.07}$	$297.17^{+75.82}_{-165.86}$	$8.58^{+8.95}_{-7.01}$	$10.35^{+5.26}_{-2.29}$
19.50–19.63	42.03	$-1.24^{+0.06}_{-0.06}$	$236.36^{+121.30}_{-123.78}$	$6.73^{+1.64}_{-1.17}$	$-1.11^{+0.16}_{-0.15}$	$258.37^{+135.76}_{-146.46}$	$7.64^{+2.31}_{-3.21}$	$7.18^{+2.60}_{-1.83}$
19.63–19.80	40.64	$-1.36^{+0.06}_{-0.07}$	$218.63^{+159.99}_{-169.43}$	$4.65^{+1.21}_{-0.80}$	$-1.32^{+0.10}_{-0.10}$	$307.79^{+245.58}_{-324.21}$	$9.27^{+2.59}_{-1.98}$	$5.13^{+1.97}_{-1.28}$
19.80–20.41	54.48	$-1.46^{+0.04}_{-0.04}$	$371.18^{+332.10}_{-358.29}$	$4.11^{+0.80}_{-0.63}$	$1.45^{+0.05}_{-0.05}$	$380.32^{+367.03}_{-395.74}$	$4.15^{+3.35}_{-2.76}$	$4.15^{+1.08}_{-0.64}$

Table 1
(Continued)

t_{start}~ t_{stop}	S	CPL			CPL plus BB			
		α	E_p (keV)	F (× 10^{-6} erg^{-1} cm^{-2} s^{-1})	α	E_p (keV)	kT (keV)	F (× 10^{-6}erg^{-1} cm^{-2} s^{-1})
(1)	(2)	(3)	(4)	(5)	(6)	(7)	(8)	(9)
20.41–22.32	70.05	$-1.43^{+0.03}_{-0.03}$	$504.41^{+352.47}_{-369.83}$	$3.48^{+0.52}_{-0.46}$	$1.43^{+0.03}_{-0.03}$	$584.74^{+543.92}_{-564.79}$	$8.00^{+5.19}_{-6.28}$	$3.64^{+1.03}_{-0.60}$
22.32–22.68	45.15	$-1.20^{+0.05}_{-0.05}$	$451.30^{+235.74}_{-243.29}$	$5.46^{+1.37}_{-0.97}$	$-1.19^{+0.05}_{-0.06}$	$446.95^{+232.74}_{-236.43}$	$3.34^{+1.97}_{-2.02}$	$5.46^{+1.42}_{-1.06}$
22.68–23.12	34.42	$-1.27^{+0.06}_{-0.06}$	$397.20^{+252.05}_{-281.53}$	$3.59^{+0.91}_{-0.76}$	$-1.23^{+0.07}_{-0.07}$	$425.78^{+280.84}_{-296.11}$	$7.49^{+4.63}_{-5.70}$	$3.65^{+1.33}_{-0.81}$
23.12–23.38	46.99	$-1.06^{+0.05}_{-0.05}$	$366.72^{+121.20}_{-115.60}$	$7.22^{+1.39}_{-1.21}$	$-1.05^{+0.05}_{-0.05}$	$366.17^{+121.97}_{-121.81}$	$3.71^{+2.99}_{-2.36}$	$7.22^{+1.63}_{-1.14}$
23.38–24.43	73.07	$-1.31^{+0.04}_{-0.03}$	$204.69^{+74.36}_{-72.34}$	$3.40^{+0.39}_{-0.34}$	$-1.26^{+0.07}_{-0.07}$	$275.87^{+141.13}_{-145.19}$	$9.95^{+1.16}_{-1.19}$	$3.71^{+0.78}_{-0.59}$
24.43–25.22	50.39	$-1.38^{+0.05}_{-0.05}$	$155.70^{+88.40}_{-85.14}$	$2.10^{+0.37}_{-0.29}$	$-1.34^{+0.07}_{-0.07}$	$162.09^{+83.15}_{-83.56}$	$5.14^{+2.88}_{-3.52}$	$2.15^{+0.49}_{-0.32}$
25.22–26.45	48.20	$-1.45^{+0.05}_{-0.05}$	$232.87^{+188.43}_{-193.61}$	$1.89^{+0.36}_{-0.27}$	$-1.44^{+0.05}_{-0.05}$	$242.03^{+179.81}_{-205.39}$	$4.41^{+4.14}_{-3.09}$	$1.95^{+0.45}_{-0.30}$
16.45–28.08	41.31	$-1.47^{+0.05}_{-0.05}$	$293.37^{+297.36}_{-312.80}$	$1.48^{+0.34}_{-0.27}$	$-1.46^{+0.05}_{-0.06}$	$301.88^{+296.86}_{-319.83}$	$4.39^{+3.80}_{-3.00}$	$1.53^{+0.46}_{-0.29}$
28.08–28.24	20.19	$-1.25^{+0.13}_{-0.12}$	$267.74^{+244.83}_{-296.94}$	$2.09^{+1.34}_{-0.58}$	$-1.23^{+0.13}_{-0.13}$	$268.14^{+229.58}_{-285.66}$	$4.15^{+3.07}_{-2.77}$	$2.19^{+1.37}_{-0.72}$
28.24–28.66	57.50	$-1.13^{+0.04}_{-0.05}$	$224.40^{+58.86}_{-60.21}$	$4.94^{+0.74}_{-0.59}$	$-1.12^{+0.05}_{-0.05}$	$225.97^{+58.90}_{-61.19}$	$4.31^{+3.45}_{-2.91}$	$5.07^{+0.69}_{-0.66}$
28.66–29.12	49.11	$-1.20^{+0.05}_{-0.05}$	$258.99^{+102.07}_{-98.42}$	$4.17^{+0.72}_{-0.58}$	$-1.25^{+0.08}_{-0.09}$	$352.09^{+344.19}_{-321.81}$	$13.04^{+6.89}_{-10.53}$	$4.80^{+2.28}_{-1.43}$
29.12–29.29	44.82	$-1.15^{+0.04}_{-0.04}$	$921.64^{+528.93}_{-544.47}$	$15.61^{+4.47}_{-3.30}$	$-1.13^{+0.05}_{-0.05}$	$887.93^{+482.86}_{-513.66}$	$4.25^{+3.28}_{-2.84}$	$15.55^{+4.73}_{-3.32}$
29.29–29.62	78.99	$-0.90^{+0.03}_{-0.03}$	$552.27^{+83.56}_{-88.34}$	$18.73^{+2.05}_{-1.95}$	$-0.89^{+0.03}_{-0.03}$	$547.49^{+92.79}_{-87.33}$	$4.21^{+3.46}_{-2.77}$	$18.56^{+2.42}_{-1.94}$
29.62–29.80	40.51	$-1.02^{+0.06}_{-0.07}$	$208.99^{+57.84}_{-59.84}$	$5.27^{+1.13}_{-0.84}$	$-1.00^{+0.07}_{-0.07}$	$216.43^{+58.28}_{-63.54}$	$6.26^{+5.92}_{-4.71}$	$5.40^{+1.50}_{-0.97}$
29.80–29.91	42.82	$-1.05^{+0.05}_{-0.05}$	$628.45^{+260.78}_{-257.91}$	$17.27^{+4.40}_{-3.23}$	$-1.04^{+0.06}_{-0.06}$	$643.37^{+244.80}_{-252.18}$	$7.32^{+7.01}_{-5.77}$	$17.65^{+4.88}_{-3.30}$
29.91–30.09	88.27	$-0.85^{+0.03}_{-0.02}$	$837.02^{+122.36}_{-117.57}$	$48.19^{+5.56}_{-5.10}$	$-0.84^{+0.03}_{-0.03}$	$838.63^{+125.15}_{-131.07}$	$5.63^{+6.73}_{-4.22}$	$48.42^{+7.01}_{-6.00}$
30.09–30.24	66.26	$-0.99^{+0.03}_{-0.03}$	$576.04^{+132.13}_{-130.54}$	$24.57^{+3.54}_{-2.95}$	$-0.98^{+0.03}_{-0.03}$	$576.49^{+128.81}_{-127.59}$	$4.28^{+2.83}_{-2.88}$	$24.83^{+3.97}_{-3.08}$
30.24–30.33	41.39	$-0.96^{+0.06}_{-0.06}$	$366.55^{+111.94}_{-115.47}$	$12.90^{+3.08}_{-2.31}$	$-0.96^{+0.06}_{-0.03}$	$373.20^{+121.94}_{-128.51}$	$6.25^{+5.64}_{-4.80}$	$13.08^{+4.13}_{-2.46}$
30.33–30.52	44.77	$-1.15^{+0.06}_{-0.06}$	$295.30^{+117.56}_{-120.25}$	$6.92^{+1.41}_{-1.17}$	$-1.10^{+0.09}_{-0.09}$	$411.47^{+214.58}_{-238.21}$	$13.03^{+2.12}_{-2.04}$	$7.59^{+2.70}_{-1.82}$
30.52–30.76	36.69	$-1.09^{+0.07}_{-0.07}$	$204.94^{+77.02}_{-77.17}$	$3.85^{+0.93}_{-0.65}$	$-1.03^{+0.11}_{-0.11}$	$211.94^{+79.62}_{-78.82}$	$5.77^{+3.37}_{-4.09}$	$3.95^{+1.31}_{-0.78}$
30.76–31.12	32.88	$-1.42^{+0.05}_{-0.05}$	$544.96^{+590.94}_{-618.25}$	$3.81^{+1.04}_{-0.77}$	$-1.40^{+0.06}_{-0.06}$	$698.69^{+810.60}_{-916.05}$	$10.16^{+5.10}_{-7.60}$	$4.22^{+1.52}_{-1.08}$
31.12–32.39	45.69	$-1.39^{+0.05}_{-0.05}$	$244.80^{+156.99}_{-166.45}$	$1.76^{+0.35}_{-0.28}$	$-1.38^{+0.05}_{-0.05}$	$245.63^{+173.34}_{-180.20}$	$2.96^{+1.58}_{-1.67}$	$1.79^{+0.42}_{-0.28}$
32.39–36.02	42.12	$-1.42^{+0.06}_{-0.05}$	$219.64^{+167.97}_{-173.18}$	$0.89^{+0.18}_{-0.14}$	$-1.41^{+0.06}_{-0.06}$	$231.66^{+173.17}_{-199.91}$	$3.93^{+3.88}_{-2.60}$	$0.92^{+0.27}_{-0.16}$
36.02–39.71	26.35	$-1.40^{+0.08}_{-0.08}$	$246.49^{+271.25}_{-294.75}$	$0.54^{+0.20}_{-0.13}$	$-1.39^{+0.08}_{-0.08}$	$262.96^{+271.00}_{-323.25}$	$3.87^{+4.06}_{-2.53}$	$0.57^{+0.33}_{-0.15}$
39.71–41.59	32.78	$-1.26^{+0.06}_{-0.06}$	$345.65^{+212.03}_{-226.86}$	$1.31^{+0.33}_{-0.24}$	$-1.24^{+0.07}_{-0.07}$	$360.09^{+245.28}_{-247.53}$	$5.28^{+4.68}_{-3.85}$	$1.36^{+0.50}_{-0.32}$
41.59–48.65	30.41	$-1.43^{+0.07}_{-0.07}$	$387.35^{+467.28}_{-570.48}$	$0.56^{+0.23}_{-0.13}$	$-1.41^{+0.07}_{-0.08}$	$389.37^{+418.51}_{-539.86}$	$3.34^{+2.79}_{-2.08}$	$0.56^{+0.30}_{-0.14}$
48.65–49.09	20.19	$-1.09^{+0.14}_{-0.14}$	$407.26^{+263.23}_{-395.91}$	$1.27^{+0.95}_{-0.45}$	$-1.02^{+0.15}_{-0.17}$	$384.17^{+225.54}_{-329.83}$	$3.92^{+3.08}_{-2.47}$	$1.30^{+1.12}_{-0.47}$
49.09–49.37	20.2	$-1.16^{+0.08}_{-0.08}$	$866.58^{+861.76}_{-912.65}$	$3.48^{+2.34}_{-1.08}$	$-1.13^{+0.10}_{-0.10}$	$834.41^{+648.04}_{-868.26}$	$3.41^{+2.16}_{-2.01}$	$3.54^{+2.46}_{-1.23}$
49.37–49.94	39.00	$-1.02^{+0.05}_{-0.05}$	$624.87^{+230.60}_{-235.23}$	$5.52^{+1.29}_{-1.02}$	$-1.01^{+0.05}_{-0.05}$	$615.52^{+217.66}_{-219.53}$	$3.04^{+1.94}_{-1.76}$	$5.61^{+1.38}_{-1.02}$
49.94–51.37	78.76	$-1.04^{+0.03}_{-0.03}$	$430^{+78.44}_{-80.13}$	$5.57^{+0.58}_{-0.49}$	$-1.03^{+0.03}_{-0.03}$	$431.46^{+76.44}_{-80.36}$	$4.29^{+3.86}_{-2.97}$	$5.64^{+0.66}_{-0.57}$
51.37–52.24	46.45	$-1.19^{+0.05}_{-0.05}$	$296.42^{+122.93}_{-125.58}$	$2.75^{+0.54}_{-0.40}$	$-1.19^{+0.06}_{-0.06}$	$333.53^{+160.82}_{-190.80}$	$7.69^{+5.89}_{-6.05}$	$2.95^{+1.08}_{-0.60}$
52.24–53.00	30.79	$-1.17^{+0.07}_{-0.07}$	$203.55^{+88.27}_{-94.78}$	$1.51^{+0.35}_{-0.30}$	$-1.15^{+0.08}_{-0.08}$	$205.28^{+93.56}_{-95.85}$	$3.38^{+2.24}_{-1.99}$	$1.54^{+0.39}_{-0.33}$
53.00–55.36	30.93	$-1.24^{+0.08}_{-0.08}$	$186.81^{+107.84}_{-109.76}$	$0.75^{+0.22}_{-0.15}$	$-1.24^{+0.09}_{-0.08}$	$206.10^{+113.66}_{-154.57}$	$4.58^{+5.46}_{-3.22}$	$0.80^{+0.33}_{-0.20}$

Table 2
Results of the Time-resolved Spectrum Analysis of GRB 180720B Fit by the Band Model

$t_{start} \sim t_{stop}$	S	Band Fitting				Band plus BB Fitting				
		α	β	E_p (keV)	F ($\times 10^{-6}$ erg^{-1} cm^{-2} s^{-1})	α	β	E_p (keV)	kT (keV)	F ($\times 10^{-6}$ erg^{-1} cm^{-2} s^{-1})
(1)	(2)	(3)	(4)	(5)	(6)	(7)	(8)	(9)	(10)	(11)
1.01–1.58	23.31	$-1.04^{+0.09}_{-0.09}$	$-2.04^{+0.28}_{-0.30}$	$1554.83^{+938.03}_{-855.61}$	$6.97^{+4.18}_{-2.59}$	$-1.02^{+0.10}_{-0.10}$	$-1.99^{+0.25}_{-0.26}$	$1381.31^{+766.12}_{-749.29}$	$3.56^{+2.47}_{-2.23}$	$6.77^{+4.59}_{-2.45}$
1.58–2.90	54.86	$-1.06^{+0.02}_{-0.02}$	$-2.63^{+0.25}_{-0.24}$	$1945.31^{+288.14}_{-280.02}$	$13.26^{+1.74}_{-1.59}$	$-1.05^{+0.03}_{-0.03}$	-- $2.62^{+0.25}_{-0.26}$	$1892.12^{+284.14}_{-278.02}$	$3.88^{+3.43}_{-2.56}$	$13.21^{+1.83}_{-1.67}$
2.90–4.08	67.51	$-0.97^{+0.02}_{-0.02}$	$-2.55^{+0.19}_{-0.19}$	$1460.27^{+171.61}_{-169.76}$	$17.04^{+2.16}_{-1.92}$	$-0.96^{+0.02}_{-0.02}$	$-2.55^{+0.18}_{-0.17}$	$1455.80^{+167.58}_{-171.69}$	$3.07^{+1.57}_{-1.81}$	$17.17^{+2.35}_{-1.85}$
4.08–6.47	110.12	$-0.93^{+0.02}_{-0.02}$	$-2.67^{+0.15}_{-0.14}$	$881.91^{+50.81}_{-49.24}$	$14.47^{+1.02}_{-1.03}$	$-0.89^{+0.02}_{-0.02}$	$-2.76^{+0.16}_{-0.16}$	$992.86^{+69.36}_{-70.46}$	$19.54^{+1.85}_{-1.87}$	$14.99^{+1.45}_{-1.17}$
6.47–7.64	66.75	$-0.99^{+0.03}_{-0.03}$	$-2.30^{+0.17}_{-0.17}$	$645.42^{+78.04}_{-78.96}$	$9.96^{+1.57}_{-1.46}$	$-0.98^{+0.03}_{-0.04}$	$-2.31^{+0.16}_{-0.16}$	$652.55^{+81.62}_{-80.85}$	$4.61^{+5.46}_{-3.30}$	$10.11^{+1.66}_{-1.40}$
7.64–7.99	53.22	$-0.90^{+0.04}_{-0.04}$	$-2.07^{+0.11}_{-0.10}$	$899.86^{+137.03}_{-142.28}$	$24.34^{+4.57}_{-3.65}$	$-0.89^{+0.04}_{-0.04}$	$-2.07^{+0.10}_{-0.01}$	$893.53^{+145.29}_{-143.31}$	$3.92^{+3.29}_{-2.58}$	$24.45^{+4.39}_{-3.87}$
7.99–8.40	73.51	$-0.89^{+0.03}_{-0.03}$	$-2.19^{+0.10}_{-0.10}$	$1033.00^{+129.89}_{-130.73}$	$34.99^{+5.25}_{-4.33}$	$-0.89^{+0.03}_{-0.03}$	$-2.18^{+0.10}_{-0.10}$	$1032.72^{+129.57}_{-123.22}$	$3.54^{+2.19}_{-2.23}$	$35.31^{+5.41}_{-4.30}$
8.40–8.73	80.46	$-0.78^{+0.03}_{-0.04}$	$-2.34^{+0.13}_{-0.12}$	$668.75^{+64.78}_{-64.38}$	$33.87^{+4.48}_{-4.11}$	$-0.78^{+0.03}_{-0.03}$	$-2.34^{+0.12}_{-0.12}$	$667.27^{+57.90}_{-59.78}$	$3.70^{+2.09}_{-2.37}$	$34.49^{+4.44}_{-4.45}$
8.73–9.33	87.60	$-0.99^{+0.03}_{-0.03}$	$-2.30^{+0.12}_{-0.12}$	$635.27^{+56.99}_{-59.32}$	$20.51^{+2.28}_{-2.04}$	$-0.92^{+0.09}_{-0.07}$	$-2.28^{+0.12}_{-0.12}$	$595.41^{+72.16}_{-75.16}$	$6.13^{+2.93}_{-4.32}$	$20.91^{+3.19}_{-2.81}$
9.33–10.34	89.19	$-0.96^{+0.03}_{-0.03}$	$-2.21^{+0.11}_{-0.11}$	$495.61^{+48.33}_{-47.38}$	$14.51^{+1.86}_{-1.69}$	$-0.95^{+0.04}_{-0.04}$	$-2.24^{+0.12}_{-0.11}$	$522.37^{+60.62}_{-63.31}$	$9.58^{+5.60}_{-7.84}$	$14.88^{+2.72}_{-2.28}$
10.34–11.02	101.89	$-0.92^{+0.02}_{-0.02}$	$-3.24^{+0.25}_{-0.25}$	$976.98^{+59.97}_{-60.17}$	$27.91^{+2.13}_{-1.95}$	$-0.90^{+0.03}_{-0.03}$	$-3.24^{+0.24}_{-0.24}$	$969.08^{+63.18}_{-63.08}$	$7.03^{+6.05}_{-5.51}$	$27.93^{+2.71}_{-2.30}$
11.02–11.27	54.80	$-0.95^{+0.04}_{-0.04}$	$-2.45^{+0.22}_{-0.22}$	$653.14^{+85.81}_{-84.81}$	$20.10^{+3.47}_{-3.06}$	$-0.91^{+0.06}_{-0.06}$	$-2.47^{+0.23}_{-0.23}$	$671.53^{+94.71}_{-95.63}$	$9.56^{+6.28}_{-7.65}$	$21.11^{+4.66}_{-3.67}$
11.27–12.33	129.40	$-0.91^{+0.02}_{-0.02}$	$-2.36^{+0.08}_{-0.08}$	$801.86^{+45.70}_{-46.62}$	$30.41^{+2.35}_{-2.16}$	$-0.90^{+0.02}_{-0.02}$	$-2.45^{+0.10}_{-0.10}$	$923.03^{+82.02}_{-79.76}$	$20.95^{+3.01}_{-2.97}$	$31.04^{+3.46}_{-2.85}$
12.33–12.64	59.43	$-0.88^{+0.06}_{-0.06}$	$-2.02^{+0.10}_{-0.10}$	$316.30^{+46.26}_{-45.65}$	$16.18^{+3.59}_{-2.89}$	$-0.84^{+0.08}_{-0.09}$	$-2.02^{+0.10}_{-0.09}$	$315.77^{+43.89}_{-44.04}$	$6.16^{+4.64}_{-4.61}$	$16.41^{+3.66}_{-3.20}$
12.64–13.33	61.19	$-1.10^{+0.04}_{-0.04}$	$-2.39^{+0.22}_{-0.22}$	$387.93^{+47.62}_{-48.97}$	$7.99^{+1.50}_{-1.24}$	$-1.09^{+0.04}_{-0.04}$	$-2.41^{+0.21}_{-0.21}$	$395.99^{+47.21}_{-47.55}$	$5.32^{+5.62}_{-3.88}$	$7.91^{+1.46}_{-1.24}$
13.33–13.50	39.65	$-0.93^{+0.06}_{-0.06}$	$-2.65^{+0.29}_{-0.30}$	$365.26^{+47.53}_{-48.84}$	$10.43^{+2.43}_{-1.70}$	$-0.91^{+0.06}_{-0.06}$	$-2.64^{+0.28}_{-0.28}$	$362.55^{+45.34}_{-45.63}$	$3.81^{+2.68}_{-2.45}$	$10.58^{+2.44}_{-1.82}$
13.50–14.19	95.12	$-0.83^{+0.03}_{-0.03}$	$-2.13^{+0.07}_{-0.08}$	$369.73^{+29.96}_{-30.83}$	$19.62^{+2.60}_{-2.29}$	$-0.82^{+0.06}_{-0.06}$	$-2.22^{+0.11}_{-0.11}$	$436.85^{+59.04}_{-57.45}$	$15.09^{+3.89}_{-3.05}$	$19.75^{+4.19}_{-3.34}$
14.19–14.41	64.62	$-0.98^{+0.03}_{-0.03}$	$-2.84^{+0.25}_{-0.25}$	$683.81^{+67.92}_{-69.97}$	$22.75^{+3.11}_{-2.65}$	$-0.92^{+0.06}_{-0.06}$	$-2.87^{+0.25}_{-0.24}$	$713.29^{+83.43}_{-82.86}$	$12.99^{+4.33}_{-4.35}$	$23.41^{+4.23}_{-3.31}$
14.41–14.79	65.23	$-0.99^{+0.05}_{-0.05}$	$-2.19^{+0.15}_{-0.14}$	$348.70^{+46.95}_{-46.47}$	$13.82^{+2.85}_{-2.50}$	$-0.97^{+0.08}_{-0.07}$	$-2.37^{+0.20}_{-0.19}$	$491.85^{+82.78}_{-82.48}$	$14.62^{+2.19}_{-2.23}$	$13.50^{+3.26}_{-2.35}$
14.79–15.05	73.87	$-0.89^{+0.03}_{-0.03}$	$-2.72^{+0.21}_{-0.21}$	$666.81^{+53.69}_{-52.83}$	$28.27^{+3.37}_{-3.13}$	$-0.89^{+0.03}_{-0.03}$	$-2.76^{+0.22}_{-0.23}$	$727.40^{+94.68}_{-92.24}$	$13.81^{+11.56}_{-12.12}$	$29.62^{+7.48}_{-4.47}$
15.05–15.50	73.57	$-0.95^{+0.04}_{-0.04}$	$-2.31^{+0.15}_{-0.15}$	$352.47^{+39.61}_{-39.11}$	$14.57^{+2.60}_{-2.13}$	$-0.91^{+0.08}_{-0.08}$	$-2.40^{+0.20}_{-0.20}$	$398.04^{+60.91}_{-65.28}$	$11.97^{+4.03}_{-2.92}$	$14.65^{+3.75}_{-3.00}$
15.50–15.84	88.96	$-0.85^{+0.03}_{-0.03}$	$-2.31^{+0.11}_{-0.10}$	$669.82^{+53.72}_{-53.24}$	$36.95^{+3.87}_{-3.71}$	$-0.82^{+0.05}_{-0.05}$	$-2.41^{+0.12}_{-0.13}$	$803.56^{+91.90}_{-61.09}$	$20.54^{+3.54}_{-3.31}$	$38.27^{+6.23}_{-5.18}$
15.84–16.29	129.66	$-0.83^{+0.02}_{-0.02}$	$-2.24^{+0.06}_{-0.07}$	$754.34^{+42.92}_{-41.45}$	$58.40^{+4.72}_{-4.07}$	$-0.83^{+0.03}_{-0.03}$	$-2.30^{+0.07}_{-0.07}$	$857.19^{+67.28}_{-66.70}$	$23.08^{+3.99}_{-3.61}$	$59.59^{+6.57}_{-5.63}$
16.29–16.44	91.86	$-0.79^{+0.03}_{-0.03}$	$-2.23^{+0.09}_{-0.09}$	$702.99^{+59.38}_{-59.38}$	$80.91^{+6.23}_{-9.18}$	$-0.80^{+0.04}_{-0.04}$	$-2.25^{+0.10}_{-0.10}$	$742.23^{+78.14}_{-91.49}$	$10.48^{+16.29}_{-8.93}$	$82.86^{+19.56}_{-12.18}$
16.44–16.63	115.87	$-0.80^{+0.02}_{-0.02}$	$-2.15^{+0.06}_{-0.06}$	$936.89^{+70.51}_{-71.44}$	$113.40^{+11.63}_{-9.61}$	$-0.81^{+0.03}_{-0.03}$	$-2.21^{+0.08}_{-0.08}$	$1101.78^{+132.83}_{-138.13}$	$26.01^{+7.19}_{-5.67}$	$116.46^{+19.69}_{-16.30}$
16.63–16.72	67.36	$-0.86^{+0.05}_{-0.04}$	$-2.21^{+0.12}_{-0.12}$	$644.98^{+85.27}_{-86.48}$	$62.24^{+10.48}_{-10.39}$	$-0.86^{+0.05}_{-0.05}$	$-2.22^{+0.13}_{-0.13}$	$661.96^{+86.03}_{-92.09}$	$5.98^{+5.16}_{-4.50}$	$61.85^{+13.83}_{-9.87}$
16.72–16.88	73.76	$-0.87^{+0.04}_{-0.04}$	$-2.15^{+0.11}_{-0.10}$	$507.51^{+58.81}_{-58.82}$	$43.01^{+6.89}_{-6.12}$	$-0.78^{+0.10}_{-0.09}$	$-2.17^{+0.10}_{-0.10}$	$514.38^{+65.55}_{-64.04}$	$10.86^{+3.38}_{-5.48}$	$42.75^{+9.77}_{-6.86}$
16.88–17.31	99.02	$-0.97^{+0.04}_{-0.04}$	$-2.22^{+0.11}_{-0.11}$	$355.68^{+34.46}_{-35.15}$	$22.22^{+3.25}_{-2.78}$	$-0.94^{+0.07}_{-0.06}$	$-2.29^{+0.13}_{-0.13}$	$395.79^{+53.88}_{-52.90}$	$12.02^{+4.41}_{-3.14}$	$22.26^{+4.85}_{-3.45}$
17.31–17.43	72.22	$-0.89^{+0.03}_{-0.03}$	$-3.07^{+0.27}_{-0.26}$	$699.55^{+53.11}_{-54.96}$	$44.12^{+4.69}_{-4.38}$	$-0.85^{+0.05}_{-0.05}$	$-3.09^{+0.26}_{-0.26}$	$748.73^{+68.34}_{-68.14}$	$16.34^{+5.40}_{-4.76}$	$45.09^{+7.41}_{-5.15}$
17.43–17.49	60.24	$-0.70^{+0.05}_{-0.05}$	$-2.45^{+0.17}_{-0.17}$	$631.78^{+65.40}_{-67.21}$	$76.62^{+13.87}_{-10.74}$	$-0.68^{+0.06}_{-0.06}$	$-2.45^{+0.17}_{-0.18}$	$642.34^{+71.48}_{-70.11}$	$8.55^{+8.82}_{-6.92}$	$78.16^{+4.31}_{-13.10}$
17.49–17.72	105.16	$-0.86^{+0.02}_{-0.02}$	$-3.26^{+0.23}_{-0.24}$	$637.57^{+34.41}_{-33.60}$	$45.57^{+3.47}_{-2.82}$	$-0.86^{+0.03}_{-0.02}$	$-3.27^{+0.24}_{-0.25}$	$642.22^{+34.67}_{-33.69}$	$6.99^{+8.44}_{-5.53}$	$45.87^{+4.31}_{-3.55}$
17.72–17.99	81.61	$-0.98^{+0.04}_{-0.04}$	$-2.48^{+0.20}_{-0.19}$	$373.13^{+36.37}_{-36.88}$	$21.32^{+3.22}_{-2.87}$	$-0.99^{+0.05}_{-0.06}$	$-2.54^{+0.21}_{-0.22}$	$411.77^{+69.60}_{-60.11}$	$11.06^{+12.02}_{-9.24}$	$21.84^{+7.12}_{-4.50}$
17.99–18.61	102.32	$-1.04^{+0.03}_{-0.03}$	$-2.61^{+0.21}_{-0.21}$	$349.46^{+23.30}_{-23.87}$	$13.90^{+1.66}_{-1.33}$	$-1.03^{+0.03}_{-0.03}$	$-2.64^{+0.20}_{-0.20}$	$362.62^{+30.06}_{-28.62}$	$8.48^{+5.52}_{-6.74}$	$14.08^{+1.89}_{-1.51}$
18.61–18.67	43.71	$-0.82^{+0.08}_{-0.08}$	$-2.92^{+0.29}_{-0.30}$	$216.65^{+18.94}_{-20.02}$	$14.98^{+2.76}_{-2.51}$	$-0.81^{+0.08}_{-0.08}$	$-2.90^{+0.27}_{-0.27}$	$218.65^{+19.90}_{-21.33}$	$4.60^{+3.58}_{-3.20}$	$15.04^{+3.26}_{-2.56}$
18.67–19.11	81.64	$-1.07^{+0.04}_{-0.04}$	$-2.40^{+0.16}_{-0.15}$	$214.35^{+17.69}_{-18.78}$	$11.04^{+1.65}_{-1.52}$	$-1.06^{+0.05}_{-0.05}$	$-2.40^{+0.16}_{-0.16}$	$215.14^{+18.95}_{-18.49}$	$4.61^{+3.86}_{-3.18}$	$11.12^{+1.94}_{-1.53}$
19.11–19.38	89.75	$-1.02^{+0.03}_{-0.03}$	$-2.72^{+0.23}_{-0.23}$	$473.31^{+39.77}_{-37.19}$	$24.73^{+3.02}_{-2.69}$	$-1.01^{+0.04}_{-0.04}$	$-2.79^{+0.23}_{-0.23}$	$521.80^{+58.46}_{-56.22}$	$14.40^{+6.25}_{-9.43}$	$25.41^{+4.53}_{-3.54}$
19.38–19.50	50.49	$-0.96^{+0.08}_{-0.08}$	$-2.34^{+0.18}_{-0.18}$	$198.23^{+26.19}_{-26.90}$	$13.17^{+3.37}_{-2.87}$	$-0.96^{+0.08}_{-0.08}$	$-2.33^{+0.17}_{-0.18}$	$200.67^{+25.66}_{-27.16}$	$4.60^{+3.93}_{-3.18}$	$13.64^{+3.87}_{-2.83}$
19.50–19.63	42.03	$-1.05^{+0.14}_{-0.15}$	$-2.16^{+0.19}_{-0.19}$	$147.98^{+39.05}_{-38.93}$	$10.13^{+5.24}_{-3.45}$	$-0.92^{+0.24}_{-0.22}$	$-2.22^{+0.21}_{-0.22}$	$164.06^{+40.66}_{-38.52}$	$5.89^{+2.21}_{-3.82}$	$10.13^{+5.24}_{-3.71}$
19.63–19.80	40.64	$-0.97^{+0.27}_{-0.27}$	$-2.03^{+0.13}_{-0.13}$	$97.68^{+36.84}_{-35.84}$	$7.96^{+10.07}_{-4.03}$	$-1.04^{+0.26}_{-0.24}$	$-2.09^{+0.17}_{-0.19}$	$124.72^{+56.98}_{-55.87}$	$4.95^{+4.13}_{-3.47}$	$7.65^{+9.94}_{-3.96}$
19.80–20.41	54.48	$-1.40^{+0.05}_{-0.05}$	$-2.13^{+0.19}_{-0.17}$	$252.83^{+60.41}_{-62.56}$	$5.67^{+1.42}_{-1.20}$	$-1.39^{+0.06}_{-0.06}$	$-2.12^{+0.18}_{-0.18}$	$249.90^{+58.98}_{-59.59}$	$3.58^{+2.62}_{-2.20}$	$5.85^{+1.51}_{-1.34}$
20.41–22.32	70.05	$-1.40^{+0.04}_{-0.04}$	$-2.23^{+0.25}_{-0.26}$	$376.14^{+89.14}_{-84.32}$	$4.35^{+0.86}_{-0.80}$	$-1.39^{+0.04}_{-0.04}$	$-2.26^{+0.26}_{-0.27}$	$404.57^{+99.41}_{-105.95}$	$5.44^{+4.66}_{-3.93}$	$4.39^{+1.19}_{-0.90}$
22.32–22.68	45.15	$-1.17^{+0.06}_{-0.06}$	$-2.39^{+0.26}_{-0.27}$	$394.57^{+72.15}_{-74.16}$	$6.91^{+1.63}_{-1.27}$	$-1.15^{+0.06}_{-0.06}$	$-2.39^{+0.25}_{-0.25}$	$384.13^{+68.19}_{-72.75}$	$3.40^{+2.03}_{-2.03}$	$6.96^{+1.44}_{-1.40}$
22.68–23.12	34.42	$-1.25^{+0.06}_{-0.06}$	$-2.50^{+0.32}_{-0.31}$	$346.63^{+69.46}_{-66.93}$	$4.21^{+1.21}_{-0.78}$	$-1.22^{+0.07}_{-0.07}$	$-2.50^{+0.30}_{-0.30}$	$374.40^{+85.21}_{-84.16}$	$6.48^{+4.94}_{-4.88}$	$4.42^{+1.58}_{-0.91}$
23.12–23.38	46.99	$-1.03^{+0.06}_{-0.06}$	$-2.55^{+0.30}_{-0.28}$	$326.22^{+45.14}_{-44.57}$	$8.88^{+2.01}_{-1.65}$	$-1.01^{+0.06}_{-0.06}$	$-2.54^{+0.28}_{-0.28}$	$322.81^{+45.12}_{-45.31}$	$3.61^{+2.27}_{-2.21}$	$8.72^{+2.02}_{-1.61}$
23.38–24.43	73.07	$-0.94^{+0.14}_{-0.13}$	$-1.97^{+0.05}_{-0.05}$	$90.71^{+14.65}_{-15.86}$	$6.00^{+2.87}_{-1.90}$	$-1.09^{+0.14}_{-0.14}$	$-2.23^{+0.19}_{-0.18}$	$179.81^{+44.04}_{-51.80}$	$8.04^{+1.66}_{-1.44}$	$5.02^{+2.47}_{-1.66}$
24.43–25.22	50.39	$-1.34^{+0.06}_{-0.07}$	$-2.53^{+0.27}_{-0.27}$	$136.34^{+17.92}_{-18.30}$	$2.59^{+0.65}_{-0.48}$	$-1.32^{+0.07}_{-0.07}$	$-2.54^{+0.26}_{-0.26}$	$139.03^{+18.27}_{-18.04}$	$4.31^{+3.03}_{-2.87}$	$2.61^{+0.72}_{-0.49}$
25.22–26.45	48.20	$-1.40^{+0.06}_{-0.06}$	$-2.40^{+0.26}_{-0.27}$	$182.47^{+34.76}_{-33.28}$	$2.38^{+0.65}_{-0.48}$	$-1.39^{+0.06}_{-0.06}$	$-2.42^{+0.27}_{-0.28}$	$185.99^{+32.60}_{-33.55}$	$3.80^{+3.33}_{-2.44}$	$2.36^{+0.61}_{-0.44}$

Table 2
(Continued)

$t_{start} \sim t_{stop}$	S	Band Fitting				Band plus BB Fitting				
		α	β	E_p (keV)	F ($\times 10^{-6}$ erg^{-1} cm^{-2} s^{-1})	α	β	E_p (keV)	kT (keV)	F ($\times 10^{-6}$ erg^{-1} cm^{-2} s^{-1})
(1)	(2)	(3)	(4)	(5)	(6)	(7)	(8)	(9)	(10)	(11)
26.45–28.08	41.31	$-1.42^{+0.05}_{-0.06}$	$-2.38^{+0.33}_{-0.34}$	$220.62^{+49.59}_{-49.75}$	$1.83^{+0.60}_{-0.43}$	$-1.41^{+0.06}_{-0.06}$	$-2.39^{+0.32}_{-0.31}$	$227.24^{+49.84}_{-48.96}$	$3.78^{+3.17}_{-2.40}$	$1.82^{+0.57}_{-0.39}$
28.08–28.24	20.19	$-1.19^{+0.15}_{-0.15}$	$-2.39^{+0.31}_{-0.30}$	$201.25^{+53.41}_{-65.76}$	$2.82^{+1.75}_{-0.97}$	$-1.18^{+0.15}_{-0.16}$	$-2.40^{+0.31}_{-0.31}$	$203.56^{+60.97}_{-64.89}$	$3.76^{+2.44}_{-2.37}$	$3.01^{+1.78}_{-1.08}$
28.24–28.66	57.50	$-1.11^{+0.05}_{-0.05}$	$-2.70^{+0.26}_{-0.27}$	$204.93^{+18.64}_{-19.25}$	$5.80^{+1.12}_{-0.77}$	$-1.10^{+0.05}_{-0.06}$	$-2.70^{+0.26}_{-0.26}$	$206.17^{+18.88}_{-18.98}$	$4.07^{+3.05}_{-2.66}$	$5.92^{+1.12}_{-0.87}$
28.66–29.12	49.11	$-1.14^{+0.07}_{-0.07}$	$-2.51^{+0.28}_{-0.30}$	$213.65^{+33.92}_{-34.69}$	$5.10^{+1.42}_{-1.04}$	$-1.17^{+0.09}_{-0.10}$	$-2.58^{+0.30}_{-0.29}$	$252.55^{+70.20}_{-65.03}$	$8.32^{+8.91}_{-6.72}$	$5.36^{+2.80}_{-1.61}$
29.12–29.29	44.82	$-1.12^{+0.05}_{-0.05}$	$-2.54^{+0.27}_{-0.28}$	$758.78^{+146.95}_{-146.75}$	$16.77^{+3.74}_{-2.60}$	$-1.10^{+0.05}_{-0.06}$	$-2.53^{+0.27}_{-0.26}$	$730.41^{+154.33}_{-147.64}$	$4.17^{+3.03}_{-2.76}$	$17.06^{+4.05}_{-3.09}$
29.29–29.62	78.99	$-0.88^{+0.03}_{-0.03}$	$-2.79^{+0.23}_{-0.22}$	$512.59^{+37.54}_{-37.16}$	$21.08^{+2.34}_{-1.91}$	$-0.86^{+0.04}_{-0.04}$	$-2.78^{+0.23}_{-0.22}$	$508.92^{+37.92}_{-38.36}$	$4.40^{+3.70}_{-2.95}$	$21.30^{+2.57}_{-2.13}$
29.62–29.80	40.51	$-0.96^{+0.09}_{-0.09}$	$-2.56^{+0.36}_{-0.34}$	$184.17^{+27.77}_{-28.62}$	$6.59^{+2.65}_{-1.64}$	$-0.96^{+0.10}_{-0.10}$	$-2.57^{+0.34}_{-0.34}$	$192.44^{+29.95}_{-31.63}$	$5.87^{+5.75}_{-4.38}$	$6.87^{+3.42}_{-1.81}$
29.80–29.91	42.82	$-1.03^{+0.06}_{-0.06}$	$-2.46^{+0.26}_{-0.26}$	$557.94^{+94.01}_{-95.34}$	$21.29^{+4.89}_{-4.10}$	$-1.02^{+0.06}_{-0.06}$	$-2.48^{+0.26}_{-0.27}$	$566.94^{+96.85}_{-101.61}$	$6.68^{+6.43}_{-5.16}$	$21.47^{+5.91}_{-4.16}$
29.91–30.09	88.27	$-0.82^{+0.03}_{-0.03}$	$-2.83^{+0.19}_{-0.20}$	$767.23^{+52.70}_{-52.09}$	$52.09^{+5.05}_{-4.58}$	$-0.82^{+0.03}_{-0.03}$	$-2.82^{+0.18}_{-0.18}$	$766.33^{+49.85}_{-49.32}$	$5.39^{+6.00}_{-3.98}$	$52.87^{+5.65}_{-4.72}$
30.09–30.24	66.26	$-0.98^{+0.04}_{-0.04}$	$-2.72^{+0.24}_{-0.25}$	$542.89^{+52.88}_{-52.84}$	$28.05^{+3.88}_{-3.23}$	$-0.97^{+0.04}_{-0.04}$	$-2.73^{+0.23}_{-0.23}$	$544.39^{+51.75}_{-52.40}$	$4.21^{+2.77}_{-2.81}$	$28.28^{+3.93}_{-3.28}$
30.24–30.33	41.39	$-0.88^{+0.09}_{-0.09}$	$-2.45^{+0.25}_{-0.25}$	$194.74^{+49.56}_{-49.10}$	$16.09^{+4.83}_{-3.59}$	$-0.87^{+0.09}_{-0.09}$	$-2.45^{+0.26}_{-0.25}$	$296.80^{+48.82}_{-49.44}$	$4.89^{+3.58}_{-3.42}$	$16.23^{+5.49}_{-3.94}$
30.33–30.52	44.77	$-0.88^{+0.18}_{-0.18}$	$-2.06^{+0.17}_{-0.15}$	$163.24^{+50.93}_{-50.23}$	$11.11^{+7.28}_{-4.61}$	$-1.02^{+0.13}_{-0.14}$	$-2.37^{+0.34}_{-0.33}$	$295.47^{+1021.99}_{-109.73}$	$10.77^{+3.54}_{-5.34}$	$9.90^{+6.23}_{-3.89}$
30.52–30.76	36.69	$-1.02^{+0.10}_{-0.10}$	$-2.40^{+0.28}_{-0.30}$	$169.83^{+28.75}_{-28.42}$	$5.24^{+1.85}_{-1.37}$	$-0.95^{+0.14}_{-0.14}$	$-2.44^{+0.27}_{-0.27}$	$175.74^{+27.76}_{-28.35}$	$5.23^{+3.24}_{-3.66}$	$5.30^{+1.87}_{-1.36}$
30.76–31.12	32.88	$-1.35^{+0.11}_{-0.10}$	$-2.46^{+0.51}_{-0.41}$	$437.08^{+191.69}_{-251.92}$	$4.60^{+2.62}_{-1.69}$	$-1.38^{+0.06}_{-0.08}$	$-2.55^{+0.33}_{-0.33}$	$627.01^{+248.73}_{-242.13}$	$9.94^{+5.09}_{-7.58}$	$4.97^{+2.15}_{-1.36}$
31.12–32.39	45.69	$-1.36^{+0.06}_{-0.06}$	$-2.47^{+0.27}_{-0.27}$	$208.95^{+36.46}_{-36.01}$	$2.16^{+0.52}_{-0.40}$	$-1.35^{+0.06}_{-0.06}$	$-2.45^{+0.27}_{-0.27}$	$206.93^{+35.89}_{-37.36}$	$2.85^{+1.43}_{-1.53}$	$2.18^{+0.61}_{-0.40}$
32.39–36.02	42.12	$-1.35^{+0.08}_{-0.09}$	$-2.25^{+0.25}_{-0.27}$	$164.77^{+41.87}_{-41.30}$	$1.24^{+0.45}_{-0.34}$	$-1.34^{+0.08}_{-0.09}$	$-2.25^{+0.25}_{-0.26}$	$164.81^{+41.84}_{-41.97}$	$3.04^{+1.63}_{-1.76}$	$1.28^{+0.50}_{-0.36}$
36.02–39.71	26.35	$-1.21^{+0.18}_{-0.18}$	$-2.07^{+0.21}_{-0.23}$	$131.05^{+49.58}_{-51.34}$	$0.89^{+0.70}_{-0.36}$	$-1.20^{+0.17}_{-0.17}$	$-2.07^{+0.20}_{-0.22}$	$134.07^{+47.99}_{-49.76}$	$2.83^{+1.52}_{-1.48}$	$0.90^{+0.64}_{-0.36}$
39.71–41.59	32.78	$-1.20^{+0.10}_{-0.10}$	$-2.21^{+0.33}_{-0.34}$	$267.69^{+82.56}_{-89.74}$	$1.88^{+0.98}_{-0.61}$	$-1.18^{+0.11}_{-0.11}$	$-2.21^{+0.33}_{-0.34}$	$279.22^{+82.75}_{-101.97}$	$4.52^{+4.30}_{-3.12}$	$1.92^{+1.14}_{-0.69}$
41.59–48.65	30.41	$-1.33^{+0.09}_{-0.10}$	$-2.17^{+0.26}_{-0.27}$	$218.17^{+72.59}_{-73.61}$	$0.74^{+0.37}_{-0.23}$	$-1.32^{+0.10}_{-0.11}$	$-2.22^{+0.29}_{-0.31}$	$230.61^{+80.36}_{-80.77}$	$3.05^{+2.17}_{-1.73}$	$0.76^{+0.36}_{-0.25}$
48.65–49.09	20.19	$-1.07^{+0.14}_{-0.14}$	$-2.44^{+0.29}_{-0.30}$	$328.75^{+91.35}_{-110.11}$	$1.66^{+0.86}_{-0.55}$	$-0.99^{+0.17}_{-0.18}$	$-2.45^{+0.30}_{-0.29}$	$303.83^{+83.51}_{-92.29}$	$3.66^{+3.06}_{-2.28}$	$1.64^{+0.91}_{-0.51}$
49.09–49.37	20.95	$-1.15^{+0.09}_{-0.10}$	$-2.26^{+0.35}_{-0.37}$	$768.96^{+280.35}_{-343.86}$	$4.83^{+2.49}_{-1.58}$	$-1.10^{+0.12}_{-0.13}$	$-2.21^{+0.32}_{-0.34}$	$690.34^{+252.91}_{-314.42}$	$3.39^{+1.94}_{-1.98}$	$4.99^{+2.56}_{-1.59}$
49.94–51.37	78.76	$-1.02^{+0.03}_{-0.03}$	$-2.69^{+0.27}_{-0.27}$	$400.24^{+31.45}_{-30.16}$	$6.49^{+0.82}_{-0.72}$	$-1.01^{+0.04}_{-0.04}$	$-2.68^{+0.26}_{-0.26}$	$397.40^{+33.09}_{-31.53}$	$3.95^{+3.61}_{-2.63}$	$6.55^{+0.90}_{-0.76}$
51.37–52.24	46.45	$-1.10^{+0.07}_{-0.07}$	$-2.17^{+0.18}_{-0.18}$	$217.90^{+38.45}_{-38.79}$	$4.13^{+1.13}_{-0.95}$	$-1.10^{+0.07}_{-0.07}$	$-2.19^{+0.20}_{-0.20}$	$227.27^{+41.73}_{-44.93}$	$4.39^{+4.35}_{-3.05}$	$4.09^{+1.35}_{-1.02}$
52.24–53.00	30.79	$-1.16^{+0.07}_{-0.08}$	$-2.71^{+0.31}_{-0.31}$	$192.02^{+26.88}_{-27.47}$	$1.77^{+0.48}_{-0.34}$	$-1.14^{+0.08}_{-0.09}$	$-2.71^{+0.30}_{-0.31}$	$192.05^{+26.76}_{-27.91}$	$3.51^{+2.44}_{-2.14}$	$1.81^{+0.52}_{-0.35}$
53.00–55.36	30.93	$-1.15^{+0.13}_{-0.12}$	$-2.40^{+0.30}_{-0.32}$	$146.70^{+33.12}_{-31.74}$	$1.02^{+0.47}_{-0.31}$	$-1.13^{+0.12}_{-0.12}$	$-2.40^{+0.29}_{-0.30}$	$146.77^{+30.43}_{-32.44}$	$3.24^{+2.13}_{-1.93}$	$1.02^{+0.47}_{-0.33}$

Table 3
Results of the Time-resolved Spectrum Analysis of GRB 180720B Fit by the Synchrotron Model

t_{start}~ t_{stop}	S	Synchrotron				Statistics
		B (G)	p	γ_{cool} (× 10^6keV)	F (× 10_{-6} erg^{-1} cm^{-2} s^{-1})	DIC
(1)	(2)	(3)	(4)	(5)	(6)	(7)
1.01–1.58	23.31	$606.65^{+138.10}_{-140.43}$	$2.41^{+0.22}_{-0.22}$	$8.73^{+5.90}_{-7.18}$	$6.39^{+5.40}_{-3.03}$	1848.51
1.58–2.90	54.86	$922.95^{+110.32}_{-116.06}$	$2.52^{+0.16}_{-0.16}$	$1.92^{+0.24}_{-0.86}$	$12.02^{+4.83}_{-3.91}$	3185.23
2.90–4.08	67.51	$1335.61^{+115.64}_{-111.50}$	$2.94^{+0.17}_{-0.17}$	$2.93^{+0.62}_{-1.81}$	$15.78^{+7.91}_{-5.01}$	3092.08
4.08–6.47	110.12	$1148.67^{+63.74}_{-66.96}$	$3.14^{+0.14}_{-0.14}$	$1.65^{+0.18}_{-0.60}$	$14.88^{+4.24}_{-2.96}$	4339.16
6.47–7.64	66.75	$631.22^{+55.04}_{-56.17}$	$2.75^{+0.16}_{-0.16}$	$2.93^{+0.34}_{-1.83}$	$10.89^{+4.71}_{-3.25}$	3093.19
7.64–7.99	53.22	$1080.82^{+107.30}_{-110.16}$	$2.79^{+0.17}_{-0.17}$	$4.73^{+2.61}_{-3.49}$	$24.12^{+16.83}_{-5.85}$	1615.11
7.99–8.40	73.51	$1324.82^{+108.84}_{-107.17}$	$2.90^{+0.14}_{-0.14}$	$2.56^{+0.79}_{-1.44}$	$34.60^{+17.29}_{-10.34}$	1906.80
8.40–8.73	80.46	$1410.61^{+104.80}_{-109.32}$	$3.50^{+0.21}_{-0.21}$	$2.96^{+1.46}_{-1.83}$	$33.34^{+19.39}_{-11.38}$	1636.28
8.73–9.33	87.60	$650.41^{+49.28}_{-47.03}$	$2.79^{+0.14}_{-0.14}$	$2.18^{+0.43}_{-1.10}$	$22.29^{+8.73}_{-6.04}$	2407.71
9.33–10.4	89.19	$569.37^{+40.87}_{-40.38}$	$2.77^{+0.13}_{-0.12}$	$2.12^{+0.28}_{-1.04}$	$15.49^{+5.20}_{-3.54}$	2993.88
10.34–11.02	101.89	$1532.65^{+94.67}_{-91.64}$	$3.84^{+0.23}_{-0.22}$	$2.06^{+0.02}_{-0.99}$	$27.69^{+8.60}_{-6.57}$	2581.53
11.02–11.27	54.80	$796.35^{+89.08}_{-85.88}$	$3.06^{+0.21}_{-0.21}$	$3.86^{+1.82}_{-2.65}$	$21.20^{+14.77}_{-7.73}$	1282.30
11.27–12.33	129.40	$1081.77^{+55.93}_{-53.46}$	$3.01^{+0.11}_{-0.11}$	$1.45^{+0.21}_{-0.40}$	$31.10^{+7.31}_{-5.06}$	3301.02
12.33–12.64	59.43	$458.84^{+46.32}_{-47.20}$	$2.86^{+0.16}_{-0.16}$	$6.94^{+3.51}_{-5.53}$	$16.50^{+11.12}_{-6.24}$	1473.26
12.64–13.33	61.19	$302.17^{+33.19}_{-32.17}$	$2.65^{+0.14}_{-0.15}$	$2.46^{+0.40}_{-1.34}$	$9.68^{+4.70}_{-3.06}$	2233.26
13.33–13.50	39.65	$581.28^{+68.06}_{-70.03}$	$3.51^{+0.29}_{-0.31}$	$7.43^{+3.73}_{-6.11}$	$11.67^{+7.38}_{-4.94}$	726.31
13.50–14.19	95.12	$645.71^{+42.69}_{-38.60}$	$3.08^{+0.15}_{-0.15}$	$3.38^{+0.98}_{-2.18}$	$19.79^{+9.71}_{-6.22}$	2476
14.19–14.41	64.62	$819.63^{+86.86}_{-87.99}$	$3.24^{+0.22}_{-0.23}$	$2.85^{+0.38}_{-1.75}$	$23.85^{+14.15}_{-7.93}$	1209.06
14.41–14.79	65.23	$366.57^{+37.00}_{-38.14}$	$2.72^{+0.16}_{-0.16}$	$2.96^{+1.11}_{-1.82}$	$15.13^{+9.31}_{-5.12}$	1623.46
14.79–15.05	73.87	$1084.00^{+89.06}_{-83.21}$	$3.53^{+0.22}_{-0.22}$	$3.72^{+1.41}_{-2.57}$	$28.32^{+16.72}_{-9.21}$	1384.58
15.05–15.50	73.57	$472.46^{+38.97}_{-39.11}$	$3.00^{+0.16}_{-0.17}$	$3.22^{+0.58}_{-2.08}$	$15.77^{+7.89}_{-4.75}$	1836.03
15.50–15.84	88.96	$1118.77^{+77.10}_{-76.07}$	$3.21^{+0.17}_{-0.16}$	$2.63^{+0.58}_{-1.51}$	$37.30^{+17.53}_{-10.09}$	1784.69
15.84–16.29	129.66	$1305.93^{+71.36}_{-69.21}$	$3.17^{+0.13}_{-0.13}$	$2.30^{+0.76}_{-1.21}$	$58.81^{+26.77}_{-15.00}$	2226.47
16.29–16.44	91.86	$1348.65^{+93.13}_{-96.30}$	$3.31^{+0.16}_{-0.16}$	$5.17^{+1.54}_{-3.95}$	$82.16^{+53.05}_{-26.66}$	1034.38
16.44–16.63	115.87	$1653.69^{+106.04}_{-102.19}$	$3.08^{+0.13}_{-0.13}$	$2.81^{+1.28}_{-1.65}$	$114.95^{+59.98}_{-35.20}$	1404.22
16.63–16.72	67.36	$992.55^{+93.38}_{-95.43}$	$3.11^{+0.21}_{-0.19}$	$5.17^{+1.42}_{-3.93}$	$63.88^{+37.83}_{-23.97}$	543.44
16.72–16.88	73.76	$761.33^{+65.89}_{-67.52}$	$3.01^{+0.19}_{-0.18}$	$4.13^{+2.35}_{-2.89}$	$43.75^{+24.84}_{-15.73}$	894.27
16.88–17.31	99.02	$433.00^{+29.55}_{-28.02}$	$2.85^{+0.13}_{-0.13}$	$2.34^{+0.31}_{-1.24}$	$23.12^{+8.92}_{-5.73}$	1950.62
17.31–17.43	72.22	$1231.18^{+112.22}_{-108.30}$	$3.85^{+0.28}_{-0.27}$	$4.09^{+0.36}_{-2.95}$	$44.85^{+24.31}_{-14.37}$	778.05
17.43–17.49	60.24	$1611.68^{+144.80}_{-148.90}$	$3.81^{+0.27}_{-0.27}$	$6.59^{+3.86}_{-5.31}$	$79.91^{+60.03}_{-30.64}$	241.92
17.49–17.72	105.16	$1316.15^{+86.15}_{-88.31}$	$4.29^{+0.24}_{-0.24}$	$2.17^{+0.81}_{-1.05}$	$46.20^{+19.82}_{-12.34}$	1483.18
17.72–17.99	81.61	$477.68^{+36.35}_{-38.14}$	$3.09^{+0.17}_{-0.17}$	$3.41^{+0.78}_{-2.29}$	$23.61^{+12.80}_{-7.74}$	1370.14
17.99–18.61	102.32	$388.20^{+28.19}_{-27.89}$	$2.97^{+0.14}_{-0.14}$	$1.98^{+0.39}_{-0.91}$	$16.42^{+5.66}_{-3.94}$	2428.75
18.61–18.67	43.71	$473.07^{+48.18}_{-50.65}$	$4.05^{+0.32}_{-0.32}$	$4.23^{+2.83}_{-3.01}$	$15.62^{+11.01}_{-5.59}$	223.68
19.11–19.38	89.75	$528.84^{+44.18}_{-42.85}$	$3.04^{+0.17}_{-0.16}$	$2.41^{+0.08}_{-1.32}$	$27.97^{+10.73}_{-7.80}$	1460.30
19.38–19.50	50.49	$300.92^{+36.10}_{-35.70}$	$3.26^{+0.21}_{-0.22}$	$7.79^{+0.75}_{-6.50}$	$14.46^{+9.86}_{-6.00}$	600.75
19.50–19.63	42.03	$170.60^{+25.20}_{-24.97}$	$2.95^{+0.19}_{-0.18}$	$6.07^{+2.99}_{-4.66}$	$10.70^{+6.60}_{-4.67}$	513.34
19.63–19.80	40.64	$123.96^{+18.14}_{-18.30}$	$2.89^{+0.19}_{-0.18}$	$4.80^{+3.29}_{-3.41}$	$7.37^{+4.73}_{-3.11}$	733.93
19.80–20.41	54.48	$73.47^{+13.65}_{-14.87}$	$2.37^{+0.13}_{-0.13}$	$2.60^{+0.44}_{-1.49}$	$6.90^{+4.56}_{-2.73}$	2031.20
20.41–22.32	70.05	$78.71^{+12.27}_{-12.34}$	$2.24^{+0.09}_{-0.08}$	$1.42^{+0.33}_{-0.36}$	$5.65^{+2.66}_{-1.87}$	3623.95
22.32–22.68	45.15	$251.25^{+42.77}_{-43.44}$	$2.65^{+0.21}_{-0.21}$	$3.69^{+1.34}_{-2.52}$	$8.55^{+5.48}_{-3.62}$	1521.97
22.68–23.12	34.42	$175.65^{+34.25}_{-32.57}$	$2.61^{+0.20}_{-0.19}$	$5.30^{+0.71}_{-4.07}$	$5.76^{+4.11}_{-2.65}$	1562.32
23.12–23.38	46.99	$400.88^{+52.35}_{-49.72}$	$3.19^{+0.26}_{-0.26}$	$6.35^{+3.75}_{-5.11}$	$10.06^{+7.49}_{-4.39}$	1143.89
23.38–24.43	73.07	$128.20^{+10.38}_{-10.38}$	$2.80^{+0.11}_{-0.11}$	$3.00^{+1.07}_{-1.77}$	$5.52^{+2.42}_{-1.66}$	2773.10
24.43-=25.22	50.39	$102.83^{+13.20}_{-12.78}$	$2.93^{+0.15}_{-0.15}$	$5.22^{+1.79}_{-4.02}$	$3.16^{+2.48}_{-1.18}$	2239.08
25.22–26.45	48.20	$87.61^{+13.51}_{-14.38}$	$2.65^{+0.14}_{-0.14}$	$3.31^{+0.95}_{-2.13}$	$3.13^{+2.05}_{-1.22}$	2841.45
26.45–28.08	41.31	$74.58^{+14.53}_{-15.39}$	$2.52^{+0.15}_{-0.15}$	$5.54^{+0.84}_{-4.32}$	$2.48^{+2.03}_{-1.13}$	3242.56
28.08–28.24	20.19	$179.72^{+44.56}_{-43.76}$	$3.09^{+0.33}_{-0.31}$	$9.22^{+7.24}_{-7.76}$	$3.05^{+3.58}_{-1.66}$	535.13
28.24–28.66	57.50	$245.61^{+28.29}_{-27.42}$	$3.22^{+0.20}_{-0.20}$	$4.42^{+0.47}_{-3.26}$	$7.12^{+4.16}_{-2.79}$	1664.68
28.66–29.12	49.11	$217.84^{+23.80}_{-24.59}$	$3.02^{+0.19}_{-0.19}$	$3.31^{+1.09}_{-2.13}$	$5.79^{+3.35}_{-1.92}$	1643.66
29.12–29.29	44.82	$447.35^{+75.97}_{-78.15}$	$2.66^{+0.23}_{-0.22}$	$3.35^{+0.88}_{-2.19}$	$19.54^{+12.03}_{-8.02}$	831.43
29.29–29.62	78.99	$952.71^{+74.75}_{-73.09}$	$3.78^{+0.22}_{-0.23}$	$2.83^{+1.12}_{-1.67}$	$21.55^{+10.76}_{-6.56}$	1593.37
29.62–29.80	40.51	$279.11^{+37.41}_{-38.57}$	$3.37^{+0.25}_{-0.26}$	$6.22^{+4.58}_{-4.79}$	$7.60^{+5.39}_{-3.31}$	838.71
29.80-29.91	42.82	$505.12^{+70.83}_{-74.40}$	$2.88^{+0.22}_{-0.23}$	$5.96^{+3.07}_{-4.73}$	$23.23^{+17.97}_{-9.45}$	426.44
29.91–30.09	88.27	$1603.20^{+119.94}_{-116.21}$	$4.01^{+0.25}_{-0.24}$	$2.64^{+1.11}_{-1.49}$	$53.63^{+26.95}_{-15.97}$	1199.12

Table 3
(Continued)

$t_{start} \sim t_{stop}$	S	Synchrotron				Statistics
		B (G)	p	γ_{cool} ($\times 10^6$ keV)	F ($\times 10^{-6}$ erg^{-1} cm^{-2} s^{-1})	DIC
(1)	(2)	(3)	(4)	(5)	(6)	(7)
30.09–30.24	66.26	$705.59^{+67.21}_{-64.90}$	$3.32^{+0.21}_{-0.22}$	$4.38^{+1.25}_{-3.20}$	$30.49^{+19.59}_{-10.18}$	837.88
30.24–30.33	41.39	$508.18^{+61.52}_{-66.45}$	$3.45^{+0.28}_{-0.28}$	$7.19^{+0.79}_{-5.89}$	$17.17^{+11.24}_{-7.16}$	341.80
30.33–30.53	44.77	$238.11^{+29.20}_{-29.67}$	$2.92^{+0.17}_{-0.18}$	$5.46^{+3.42}_{-4.16}$	$10.61^{+7.44}_{-4.34}$	874.62
30.52–30.76	36.69	$231.86^{+34.12}_{-36.64}$	$3.22^{+0.26}_{-0.26}$	$6.03^{+3.54}_{-4.65}$	$6.26^{+4.40}_{-3.01}$	1028.91
30.76–31.12	32.88	$116.15^{+22.63}_{-22.03}$	$2.52^{+0.16}_{-0.16}$	$6.73^{+1.96}_{-5.47}$	$5.47^{+4.10}_{-2.48}$	1371.09
31.12–32.39	45.69	$107.85^{+18.37}_{-18.72}$	$2.66^{+0.17}_{-0.16}$	$3.15^{+0.48}_{-2.00}$	$2.78^{+2.14}_{-1.16}$	2936.01
32.39–36.02	42.12	$93.78^{+15.04}_{-15.01}$	$2.69^{+0.15}_{-0.14}$	$4.43^{+2.23}_{-3.13}$	$1.47^{+0.99}_{-0.59}$	4408.23
36.02–39.71	26.35	$100.09^{+19.32}_{-18.58}$	$2.74^{+0.15}_{-0.17}$	$11.22^{+5.90}_{-9.58}$	$0.94^{+0.78}_{-0.43}$	4363.42
39.71–41.59	32.78	$148.01^{+26.37}_{-27.36}$	$2.53^{+0.15}_{-0.16}$	$5.86^{+3.02}_{-4.53}$	$2.29^{+1.78}_{-1.00}$	3389.04
41.59–48.65	30.41	$90.78^{+21.63}_{-22.02}$	$2.52^{+0.16}_{-0.17}$	$5.92^{+1.74}_{-4.60}$	$0.98^{+0.90}_{-0.51}$	5324.66
48.65–49.09	20.19	$347.92^{+74.88}_{-74.82}$	$3.23^{+0.35}_{-0.35}$	$12.54^{+11.56}_{-10.91}$	$1.70^{+1.84}_{-0.86}$	1404.79
49.09–49.37	20.19	$385.94^{+97.99}_{-96.79}$	$2.73^{+0.30}_{-0.32}$	$8.65^{+6.82}_{-7.14}$	$4.69^{+4.68}_{-2.51}$	1032.68
49.37–49.94	39.00	$625.55^{+83.09}_{-80.88}$	$3.09^{+0.28}_{-0.27}$	$5.31^{+1.90}_{-4.09}$	$7.14^{+5.68}_{-3.01}$	1976.49
49.94–51.37	78.76	$457.25^{+38.49}_{-37.47}$	$3.00^{+0.17}_{-0.17}$	$2.27^{+0.37}_{-1.18}$	$7.76^{+3.35}_{-2.12}$	3321.90
51.37–52.24	46.45	$202.09^{+26.90}_{-25.64}$	$2.75^{+0.18}_{-0.17}$	$5.10^{+2.35}_{-3.83}$	$4.68^{+3.24}_{-1.81}$	2406.34
52.24–53.00	30.79	$215.45^{+35.65}_{-35.54}$	$3.27^{+0.29}_{-0.27}$	$5.94^{+2.39}_{-4.66}$	$2.16^{+1.69}_{-0.99}$	2143.60
53.00–55.36	30.93	$161.43^{+23.49}_{-23.11}$	$3.10^{+0.24}_{-0.22}$	$5.17^{+3.27}_{-3.81}$	$1.11^{+0.90}_{-0.47}$	3677.91

$\log(E_p)-a$, $\log(F)-p$, $\log(F)-B$, and $\log(B)-p$. Table 5 gives the results of a Spearman rank correlation analysis. From Table 5, it can be seen that all of the parameter pairs reveal strongly correlated relationships.

The left panel in Figure 9 shows the correlation $\log(F)-a$. Previous analyses (Borgonovo & Ryde 2001; Firmani et al. 2009; Ghirlanda et al. 2010; Yu et al. 2018) revealed that there are three main types of $\log(F)-a$ relationships: non-monotonic relationships (contains positive and negative power-law segments, typically with apparent discontinuities at the peak flux), a monotonic relationship (described by a single power law), and no evident trend. The $\log(F)-a$ in the time-resolved spectrum of GRB 180720B shows a close positive monotonic correlation ($r = 0.85$, $p < 10^{-4}$). Figure 9 shows the correlation between $\log(F)$ and $\log(E_p)$. The relationship between the two is similar to that illustrated in Figure 9, showing a close positive monotonic correlation ($r = 0.65$, $p < 10^{-4}$). Another meaningful relationship, the relationship of $a-\log(E_p)$, has been studied in previous papers (Lloyd et al. 2000; Kaneko et al. 2006; Chhotray & Lazzati 2015; Burgess & Ryde 2015). As shown in Figure 9, it has a similar relationship with $\log(F)-a$, that is, a close monotonic positive correlation ($r = 0.44$, $p < 10^{-4}$). Figure 10 shows the relationship of the synchrotron model parameters: $\log(F)-p$, $\log(F)-B$, and $\log(B)-p$; the three relationships are all monotonic positive correlations, and the correlation coefficients are: $r = 0.51$ ($p < 1 \times 10^{-4}$), $r = 0.87$ ($p < 1 \times 10^{-4}$), and $r = 0.56$ ($p < 1 \times 10^{-4}$).

4.5. Empirical Model versus Physical Model

As shown in Figure 11, we compare the DIC of the CPL model, the Band model, and the synchrotron model. It can be seen that the Band model and the synchrotron model both give the same DIC, while the CPL model and the synchrotron model are slightly different. This shows that the physical model proposed by Burgess et al. (2020) successfully fits the typical spectra, and these spectra can be well fitted by the empirical Band function. In Figure 12, we make a comparison between the energy spectrum fitted by the three models and the fitting residuals at a time interval of 16.29–16.44 s as an example. This again clearly shows that all three models adequately represent the data. Figure 13 shows the model curves of the Band function, CPL function, and synchrotron model. It can be seen that the two curves of the Band function and the synchrotron model are basically the same in the GBM channel. The CPL function is the same as the other two functions in the energy range of $10 \sim 10^3$ keV and shows a significant difference after 10^3 keV; that is, it cut off in the high energy range. Our results seem to reveal that the synchrotron model can also interpret the Band function in the GBM channel (Zhang et al. 2016).

We systematically checked the correlation between the Band model parameters and the synchrotron model parameters. As shown in Figure 14, we find that there are three parameter pairs that have a strong correlation: $\alpha - p$ ($r = 0.65$, $p < 1 \times 10^{-4}$); $\log(B)-a$ ($r = 0.83$, $p < 1 \times 10^{-4}$); and $\log(B)-\log(E_p)$ ($r = 0.82$, $p < 1 \times 10^{-4}$). This indicates that the observed spectral characteristics can be explained by changes in jet magnetization and electron injection parameters (Zhang et al. 2016).

5. Conclusion and Discussion

GRB 180720B is a very bright long burst with a multi-pulse structure. We apply the Bayesian blocks method to perform the time slicing and use two empirical photon models (CPL and Band models) and a physical model (synchrotron model) to perform detailed time-resolved spectra. A total of 73 spectra were obtained, and their properties are studied. We reach some interesting conclusions about GRB 180720B.

First, our studies reveal that 73 time-resolved spectra can be well fit by the CPL and Band models. Moreover, with the addition of thermal components, the fitting statistics are significantly improved, which reveals that for GRB 180720B,

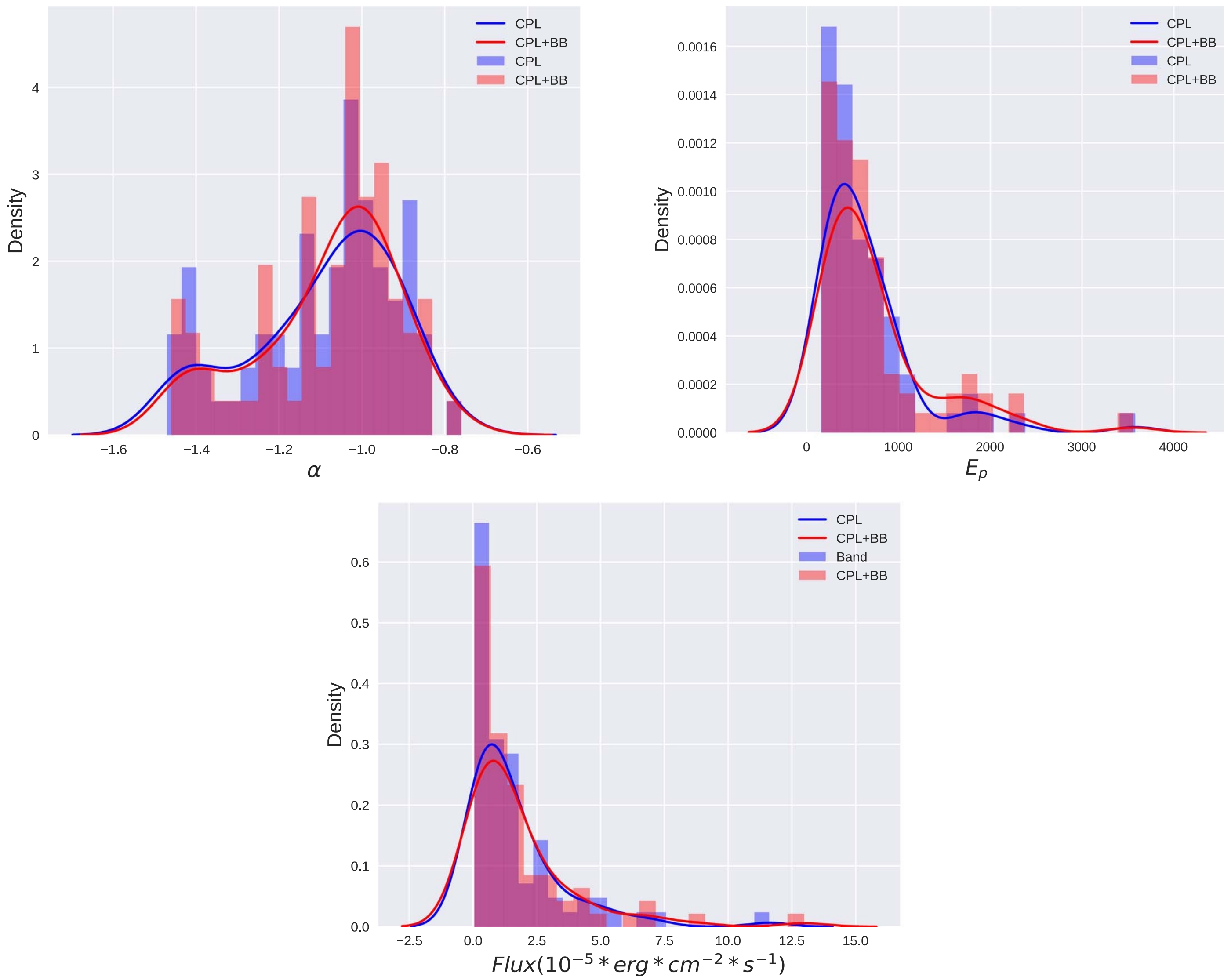

Figure 2. Parameter distribution of the CPL and CPL+BB fitting parameters. The curves represent the KDE of the distributions.

there are significant thermal components (~40%). The spectrum with thermal components (ΔDIC < −10) mainly focuses on the beginning (0 ~ 20 s) and peak phases of the pulse. The thermal component gradually decreases, indicating that Fermi multi-pulse GRB may transition from a material-dominated fireball to a magnetic-dominated Poynting flux. Generally, the GRB jet is likely to be a hybrid system, with both a hot fireball component and a cold Poynting flow component (Gao & Zhang 2015). Some bright bursts (such as GRB 91111824) show thermal-like time-resolved spectra at the beginning or near the peak of the pulse, and nonthermal time-resolved spectra appear in subsequent pulses, which may indicate a gradual change in jet composition (Ryde et al. 2010). Zhang et al. (2018) reported the spectral characteristics of GRB 160625B with three sub-bursts and found that the spectra between different sub-bursts have different physical origins; for the first time, it is proposed that from the early stage to the later stage of the burst, it is from the fireball to the Poynting flux dominant outflow transition. In addition, Li (2019b) analyzed the time-resolved spectra of four bright GRBs (GRB 140206B, GRB 140329B, GRB 150330A, and GRB 160625B) and found that the BB component mainly appeared at the beginning of the pulse, followed by nonthermal synchrotron radiation. Fireball-based and Poynting flux are both physical models at the two extremes. Another possibility of GRB's jet composition is a hybrid system, which has both thermal fireball and Poynting flux components. Gao & Zhang (2015) provided a more comprehensive description when explaining the origin of the GRB jet composition. They believe that the GRB jet composition is a hybrid jet. Li (2019a) used this method to analyze eight Fermi GRBs and found that the hybrid jet problem can explain most outbreaks (possibly all). Therefore, GRB 180720B also supports hybrid jet model by performing the time-resolved spectral analysis.

Second, it is found that the value of the low-energy index α of GRB 180720B does not exceed the so-called synchrotron radiation dead line for both with and without thermal components. As is known, the typical spectrum of GRB can be described by the main nonthermal components (Band function or CPL), some of which have additional thermal components (Planck function). In the previous analysis, the low-energy index α is usually used to infer the radiation mechanism of prompt emission. When α > −2/3 (the dead line), synchrotron radiation cannot generate the spectrum. Burgess et al. (2020) found that the spectral index α fitted by

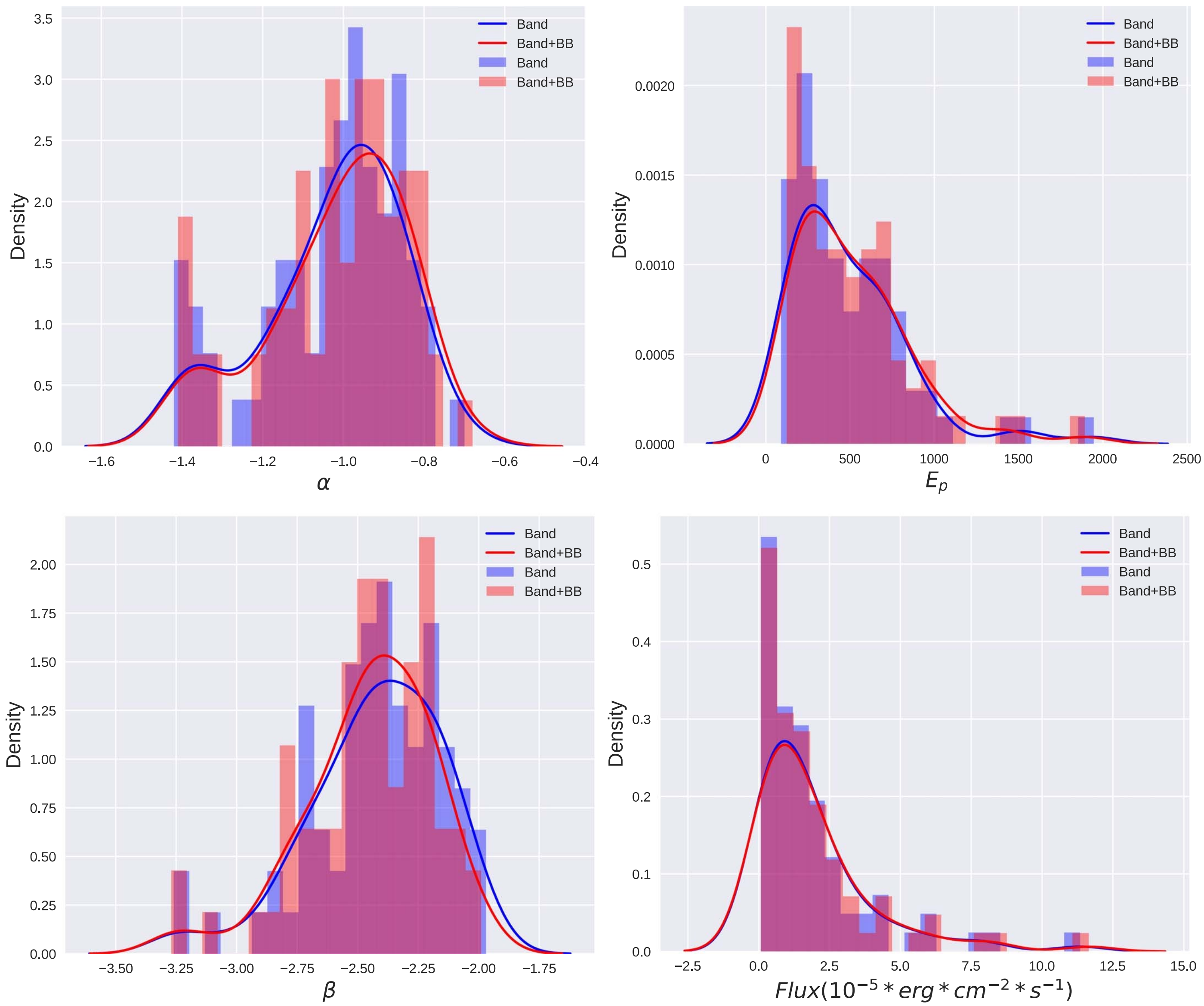

Figure 3. Parameter distribution of the Band and Band+BB fitting parameters. The curves represent the KDE of the distributions.

Table 4
The Values of the Average and Standard Deviation of the Parameter Distributions

Model	α/p	β/B(G)	E_p/γ_{cool}(keV)	F(× 10^{-5} erg^{-1} s^{-1} cm^{-2})
CPL	−1.09 ± 0.17	L	644.32 ± 557.34	1.64 ± 1.94
CPL+BB	−1.08 ± 0.17	L	618.87 ± 522.61	1.79 ± 2.21
Band	−1.03 ± 0.17	−2.42 ± 0.27	489.11 ± 343.17	1.88 ± 2.06
Band+BB	−1.01 ± 0.17	−2.45 ± 0.26	509.59 ± 337.60	1.91 ± 2.10
Synchrotron	−3.03 ± 0.41	587.08 ± 456.52	4.44 ± 2.24	1.97 ± 2.09

the Band function exceeds −2/3, but the synchrotron model can fit well. The α of GRB 180720B does not exceed the synchrotron radiation dead line. However, the introduction of thermal components can improve the fitting results, indicating that it is not accurate to infer thermal radiation from the hard spectral index (Zhang et al. 2016; Burgess et al. 2020). Based on the α of GRB 180720B not exceeding the synchrotron radiation dead line and there is a thermal component in the spectrum, so we used the synchrotron model to fit the time-resolved spectrum, and found that in the GBM channel, the Band function and the synchrotron model have almost the same model curve. We also fit the time-resolved spectra with the synchrotron model and find that the model curves of the Band function and synchrotron model are almost the same in the GBM channel. Therefore, our results also reveal that the synchrotron model seems to be consistent with the Band function in the GBM channel and the synchrotron model can also explain the origin of the Band function (Zhang et al. 2016).

Third, we also find that the empirical model parameters α, E_p and synchrotron model parameters p, B of GRB 180720B show

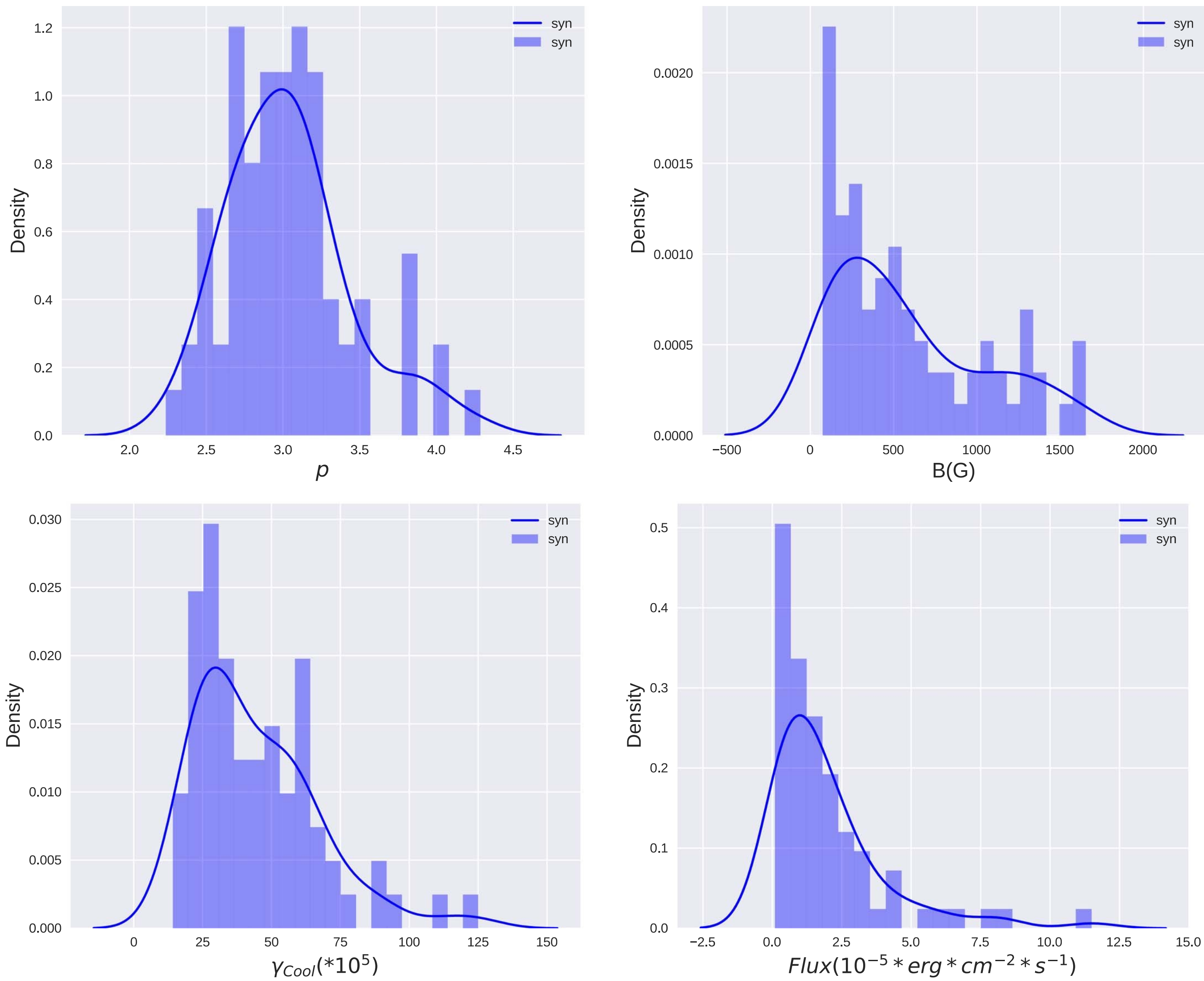

Figure 4. Parameter distribution of synchrotron fitting parameters. The curves represent the KDE of the distributions.

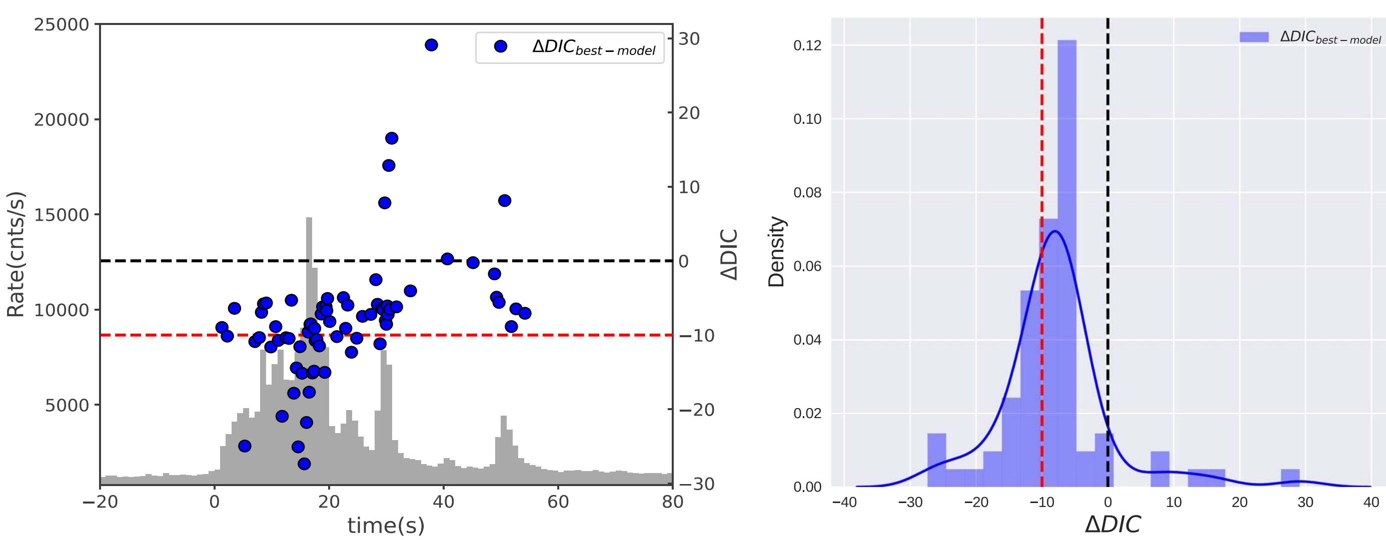

Figure 5. ΔDIC evolves and distributes with a pulse. The panel on the left shows the distribution of the DIC in the pulse. The figure on the right represents the distribution of KDE. The black and red lines indicate ΔDIC = 0 and ΔDIC = − 10, respectively. Exceeding the black line means that the BB component has been added to improve the fitting statistics. Exceeding the red line suggests strong evidence that there is a BB component.

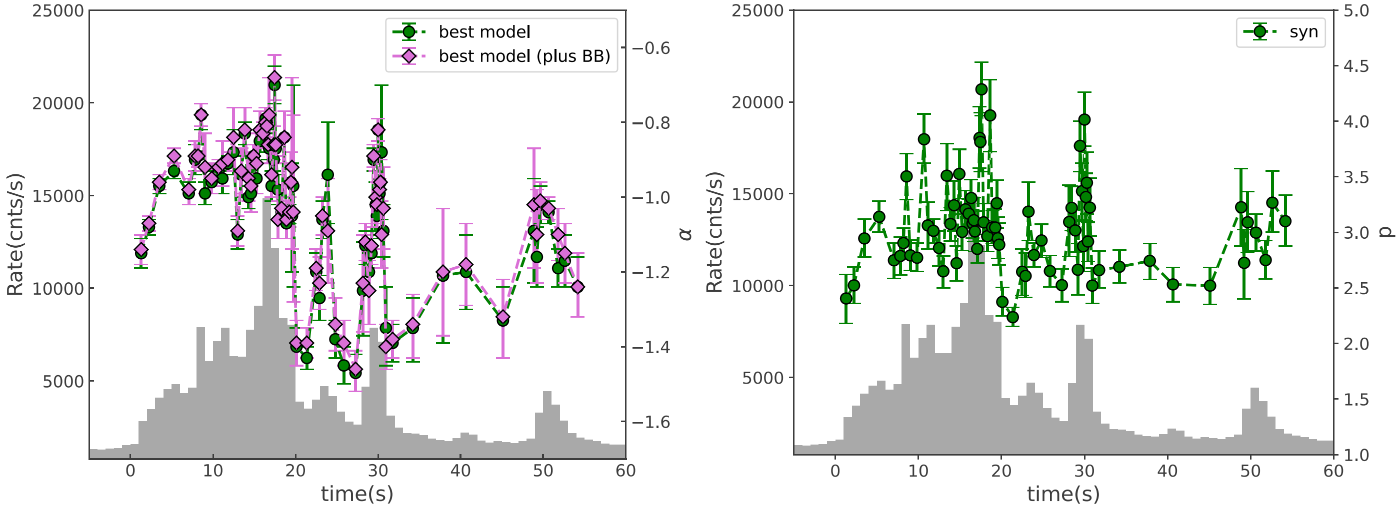

Figure 6. The evolution of the low-energy spectrum index α (left panel) and the electronic spectrum index p (right panel) of the best model and synchrotron model, where the pink and green data points represent the model with thermal component (BB) and the model without a thermal component.

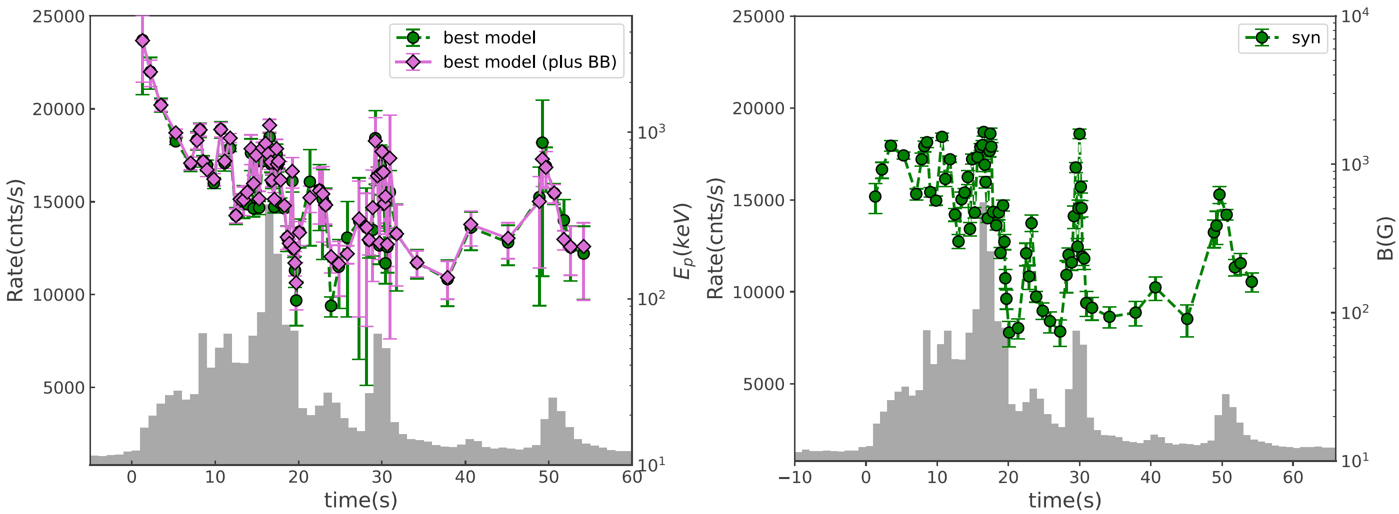

Figure 7. The evolution of the peak energy E_p (kiloelectronvolts) of the best model (left) and the magnetic field strength B(G) of the synchrotron radiation model (right panel).

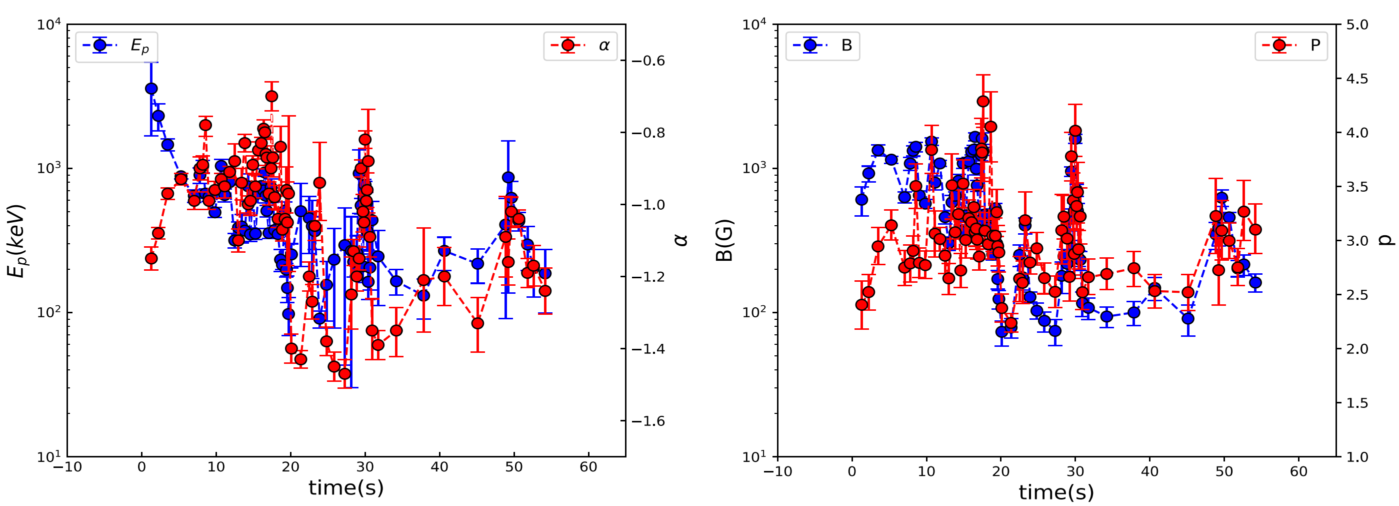

Figure 8. The evolution of E_p–α and B–p over time. The panel on the left shows a comparison of the evolution patterns of α (red) and E_p (blue) over time. The figure on the right shows a comparison of the evolution patterns of the synchrotron model parameters p (red) and B (blue) over time.

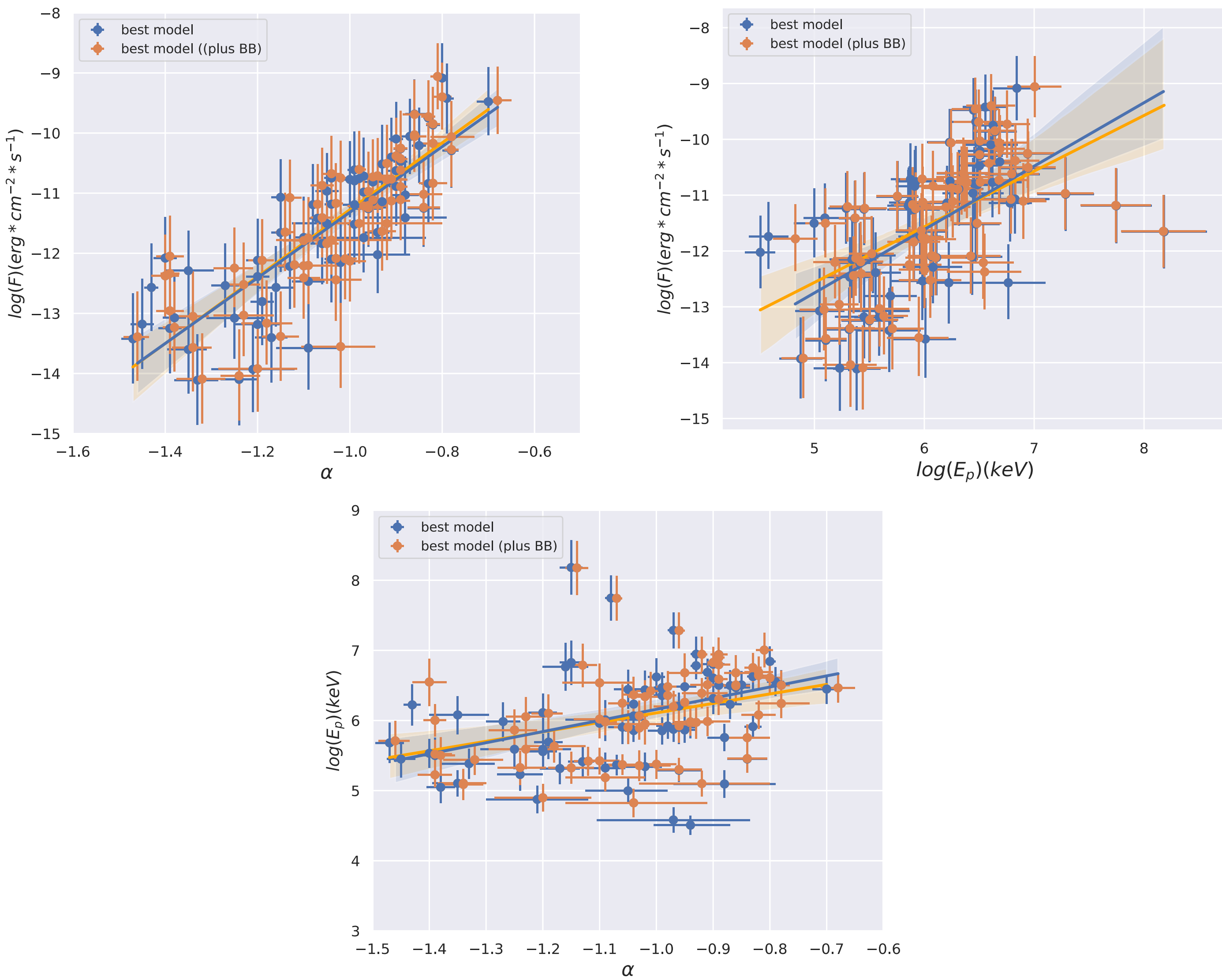

Figure 9. The relationship between the best empirical model parameters including $\log(F)-\alpha$, $\log(F)-\log(E_p)$, $\log(E_p)-\alpha$. The orange point is the fitting parameter of adding the BB component. The shading indicates a confidence level of 0.95.

a special spectral evolution model. The evolution model of E_p and α in GRB 180720B is different; α shows the flux tracking mode, and at the beginning of the burst, E_p has a hard-to-soft evolution mode followed by a flux tracking mode. The synchrotron model parameters p and B appear to be the double tracking model. Significant spectral evolution can usually be observed for multi-pulse bright bursts, which provides more clues about GRB prompt emission. An exciting feature is the relationship between E_p, α, and flux in the GRB pulse. Previous studies have found that parameters usually have two types of evolution patterns: the first type shows an evolution pattern from hard to soft, which means that E_p decreases throughout the pulse, even during the rising phase of the pulse (Norris et al. 1986). The second type is the tracking mode, which rises and falls with the flux (Golenetskii et al. 1983). The superposition of hard-to-soft evolution pulses may cause apparent tracking behavior (Lu et al. 2012). It has been proposed that all pulses may be consistent with a hard-to-soft evolutionary model (Hakkila & Preece 2011). However, (Li 2019a) found by studying large-sample multi-pulse GRB that, for the evolution of E_p, about two-thirds of the pulses show flux tracking patterns, and about one-third of the pulses show hard to soft. For α evolution, flux tracking accounted for 65% of pulses and hard to soft accounted for 25% of pulses. Our results indicate that spectral evolution may be the key to understand GRB radiation physics and the origin of various observed spectral-energy relationships (Ghirlanda et al. 2004; Liang & Dai 2004; Liang & Zhang 2005). Below we will discuss the possible reasons for the behavior of α, E_p, and B and p flux tracking, respectively.

The curvature effect can explain the evolution of E_p (Zhang & Mészáros 2002). Based on the typical energies $E_p = DE'_p/(1+z)$ in the decay stage, specific luminosity $L_\nu = D^2 L'_{\nu'}$ and bolometric luminosity $L_{\rm iso} = D^4 L'_{\rm iso}$ (D is the Doppler factor), we can get $E_p \propto L_{\rm iso}^{1/4}/(1+z) f(E'_p, L'_{\rm iso})$, $E_p \propto L_\nu^{1/2}/(1+z) f'(E'_p, L'^{1/2}_{\nu'})$, where $f(E'_p, L'_{\rm iso}) = E'_p/L'^{1/4}_{\rm iso}$, $f'(E'_p, L'_{\nu'}) = E'_p/L'^{1/2}_{\nu'}$. The relationship between $E_p \propto L_{\rm iso}^{1/4}$ and $E_p \propto L_\nu^{1/2}$ can give E_p flux tracking behavior.

In the standard synchrotron model, a similar relationship can be derived. The peak energy can be written as $E_p \propto L^{1/2} \gamma^2_{e,\rm ch} R^{-1} (1+z)^{-1}$, where L is the wind luminosity

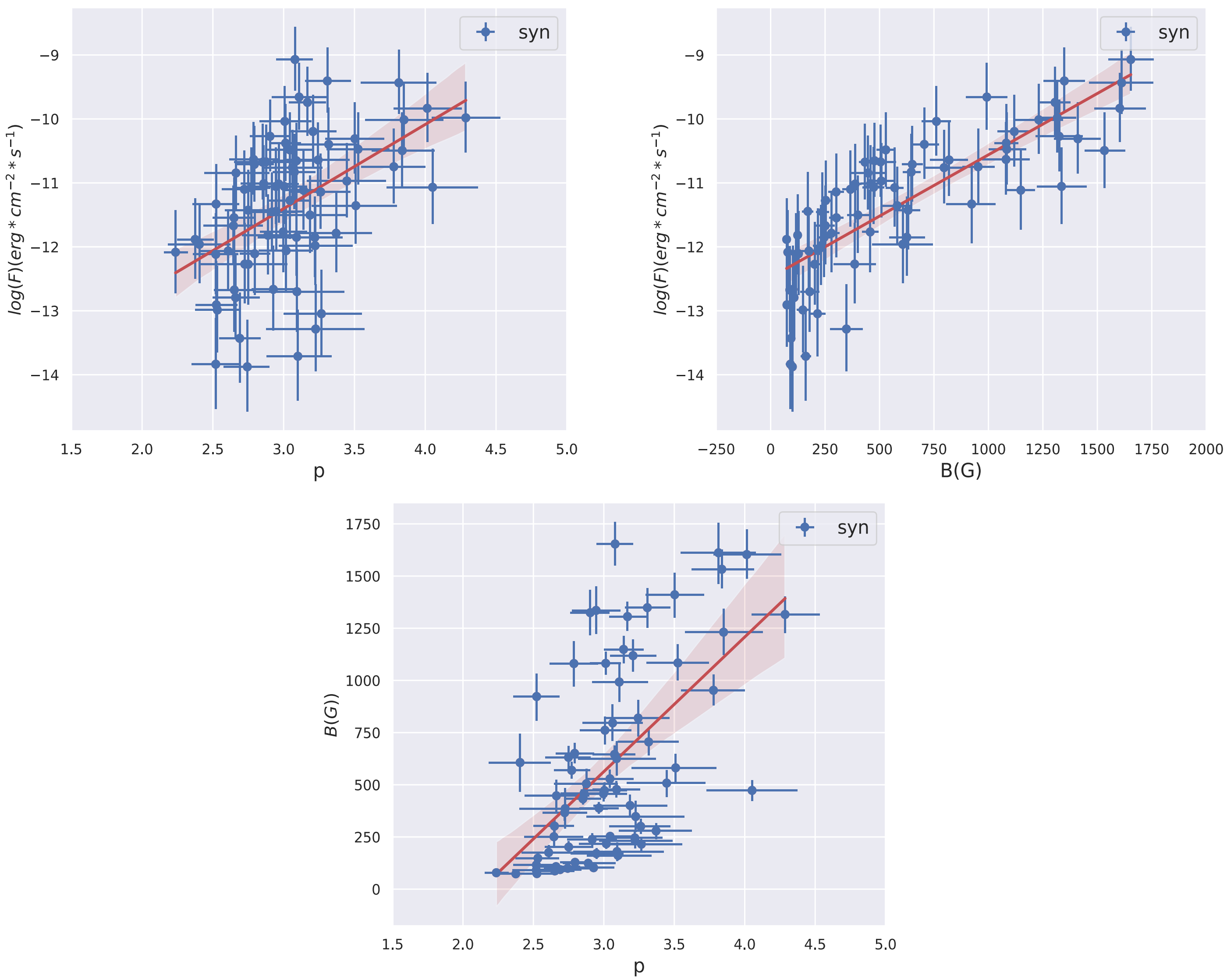

Figure 10. The relationship of the synchrotron model parameters $\log(F)$–p, $\log(F)$–B, and $\log(B)$–p.

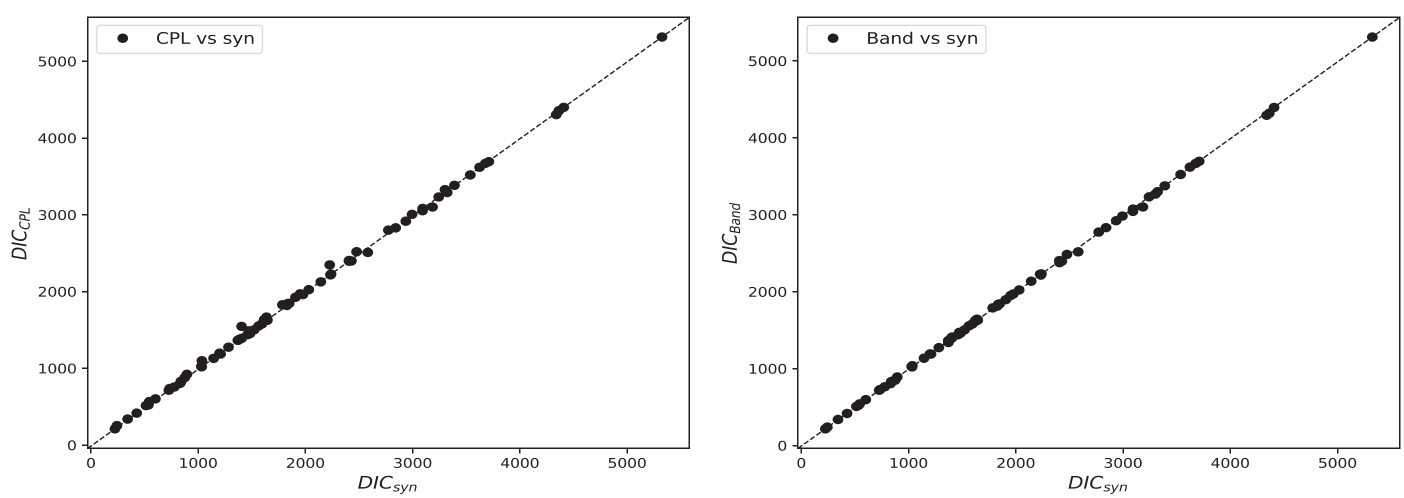

Figure 11. Comparison of 73 spectral fitting statistics of the DIC of the CPL model, Band model, and synchrotron model, and the shape of the energy spectrum.

of the projectile, $\gamma_{e,ch}$ is the electronic Lorentz factor of the radiation area, and R is the radiation radius (Zhang & Mészáros 2002). The flux tracking behavior can be given by the relationship of $E_p \propto L^{1/2}$. It can also be seen from the above relationship that flux is related to the evolution of shock wave intensity ($\gamma_{e,ch}$) in the shock wave traversing process and

Table 5
The Spearman Correlation Coefficient of the Parameter Pairs

Model	F − α(F − p)		F − E_p(F − B)		α − E_p(B − p)	
	r	p	r	p	r	p
Nonthermal	0.85	$=10^{-4}$	0.65	$=10^{-4}$	0.44	$=10^{-4}$
Nonthermal+BB	0.85	$=10^{-4}$	0.70	$=10^{-4}$	0.50	$=10^{-4}$
Synchrotron	0.51	$=10^{-4}$	0.87	$=10^{-4}$	0.56	$=10^{-4}$

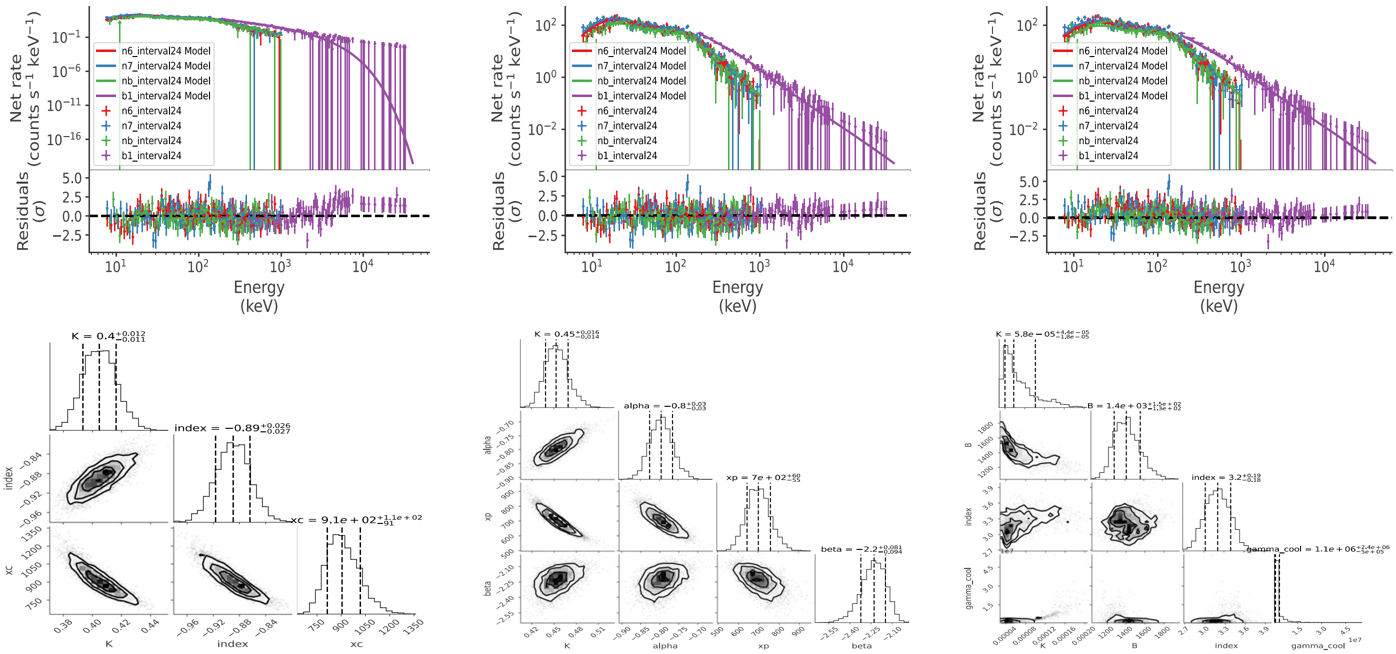

Figure 12. Comparison of the CPL model, Band model, and synchrotron model with an interval of 16.29 ~ 16.44 s.

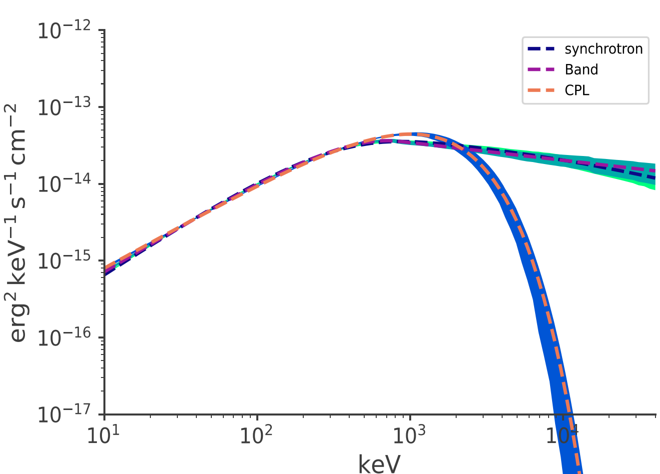

Figure 13. Comparison between the two theoretical models in Figure 12. The blue dotted line, purple dotted line, and orange dotted line represent the energy spectrum shapes of the synchrotron model, the Band model, and the CPL model, respectively, and the shaded part represents the 0.68 confidence interval.

the number of electrons being shocked. It shows that the synchrotron model can produce E_p flux tracking behavior (Uhm et al. 2018; Li et al. 2019).

On the other hand, the dissipative photosphere model attributes E_p to the temperature of the photosphere (Pe'Er et al. 2006; Lazzati & Begelman 2009; Ryde et al. 2011; Ruffini et al. 2013, 2014; Meng et al. 2018). In the range of $r_{ph} > r_s$, $T_{ph} \propto L_w^{1/4} r_0^{-1/2} (r_{ph}/r_s)^{-2/3}$, $r_s = \eta r_0$ and $r_{ph} \sim L_w \eta^{-3}$, the observer temperature can be expressed as $E_p \propto T_{ph} \propto L_w^{-5/12} r_0^{1/6} \eta^{8/3}$ (Deng & Zhang 2014). From the above formula, it can be concluded that if η and r_0 are constants, and E_p and L_w are inversely related. This trend seems consistent with the hard-to-soft evolution pattern of the pulse rising phase.

GRB 180720B shows a hard-to-soft evolution model in the early stage of the pulse, which is consistent with the interpretation of the photosphere model. The E_p flux tracking mode can be explained by the synchrotron radiation model in the subsequent pulse. In the same GRB, two different evolution patterns appear, indicating the gradual change of jet composition and evidence that the multi-pulse GRB 180720B jet may transition from a material-dominated fireball to a magnetic-dominated Poynting flux. Regarding the tracking behavior of α, Li et al. (2019) pointed out that α becomes harder during the rise phase, which indicates that electrons are evolving from the fast cooling zone to the slow cooling zone. In the decay phase, α becomes softer in observation. The curvature effect may control the decay phase of the wide pulse (Uhm & Zhang 2015, 2016).

In the fitting parameters of the synchrotron model of GRB 180720B, both B and p have the behavior of double-flux tracking. In the synchronous model, the observed flux is given by $F = \sigma_T c \Gamma^2 \gamma_e^2 B^2 N_e / 24\pi^2 d_L^2$, where B is the magnetic field intensity in the comoving frame, N_e is the number of radiating electrons, and γ_e is electrons to be accelerated to some characteristic Lorentz factor (Iyyani et al. 2016). We can get

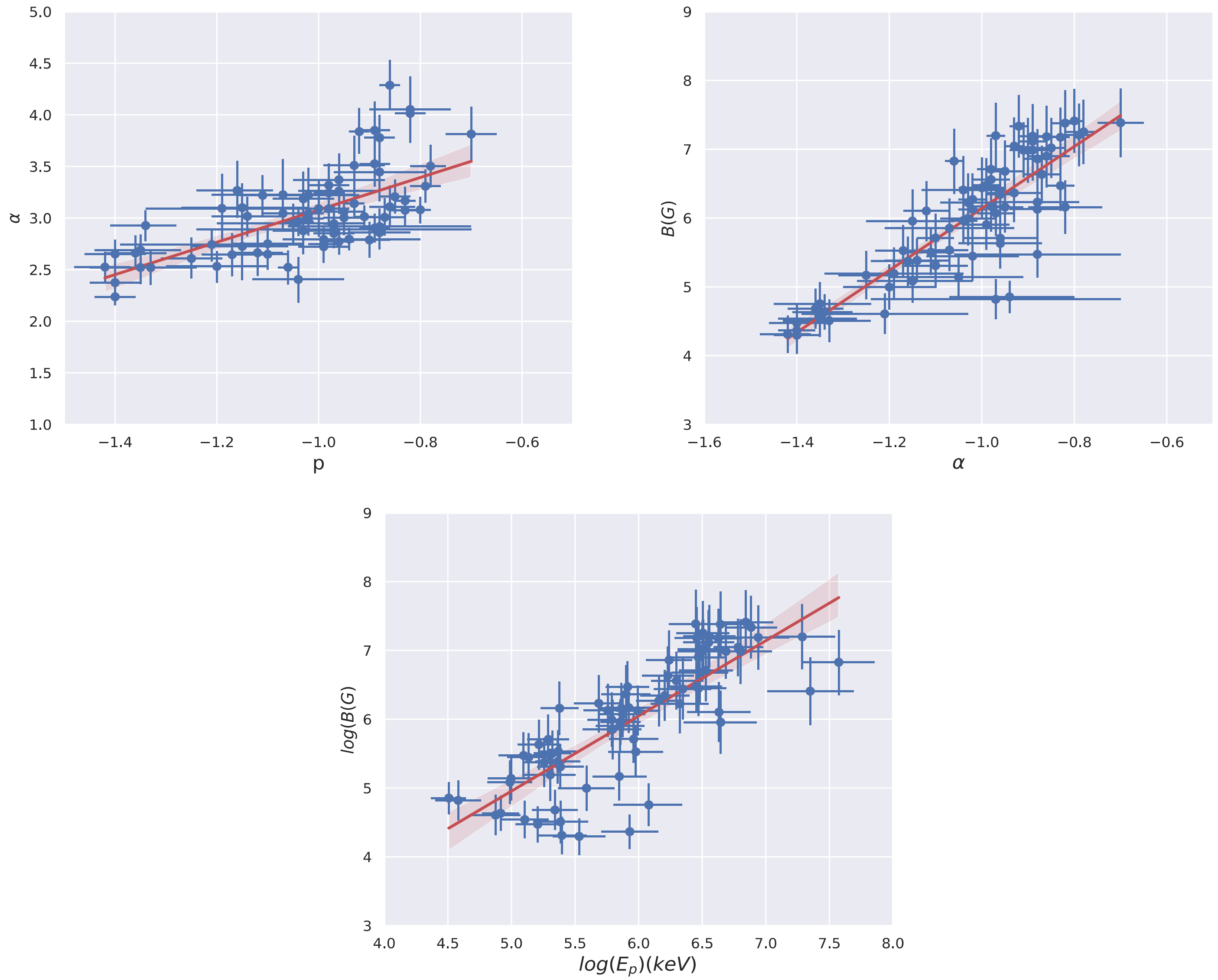

Figure 14. Parameter relationship between the physical model and empirical model.

$F \propto \Gamma^2 B^2 N_e$, and we can know that F and B have a strong correlation through the previous correlation analysis. This may be that B has the behavior of flux tracking, but the specific physical process is not known yet. We know that the electron spectrum index p of the synchronous model can be converted into the photon spectrum index by $F_\nu = \nu^{-(p-1)/2-1}$, then we can get $\alpha = -(p-1)/2 - 1$. Through analysis, we also get that p is strongly correlated with F and α; they have similar tracking behavior, and we guess that they have the same physical origin. The physical reason why both p and B have flux tracking behavior is still not apparent. Here we only analyzed one burst. To explain this phenomenon well, a large number of samples should be studied, and further studies should be conducted through numerical simulation and other methods.

In summary, the energy spectrum components and energy spectrum parameters of GRB 180720B in the prompt emission phase have interesting evolutionary characteristics. First, we introduced the BB component based on the empirical model. We present that adding the BB component improved the fitting statistics, indicating that the spectrum of GRB 180720B contains thermal components. Different from other results, the thermal components in the GRB 180720B are not only distributed at the beginning but at the peak phase of the pulse. Second, we conducted a detailed time characteristic analysis of the spectral parameters and found that α has a strong correlation with flux and exhibits flux tracking behavior, which is the same as the result found by Duan & Wang (2019). However, the time evolution behavior of E_p is different from their results. They proposed showing the flux tracking behavior throughout the pulse. But our result is that at the beginning (0 ~ 7 s) of the pulse, there is a hard-to-soft evolution mode, followed by a flux tracking mode. The difference may be that the method of slicing the bin is different. The time bin of the traditional signal-to-noise ratio method is relatively rough, which may conceal the physical characteristics. Inspired by these strong correlations, we checked the Amati relationship of the burst. As shown in Figure 15, the burst conforms to the Amati relation, but the introduction of the BB component weakens the Amati relation. Third, we use the Bayesian method to perform detailed time-resolved analysis. We present that the low-energy photon index α in the prompt emission phase does not exceed the synchrotron dead line, which is consistent with the results of Duan & Wang (2019), and

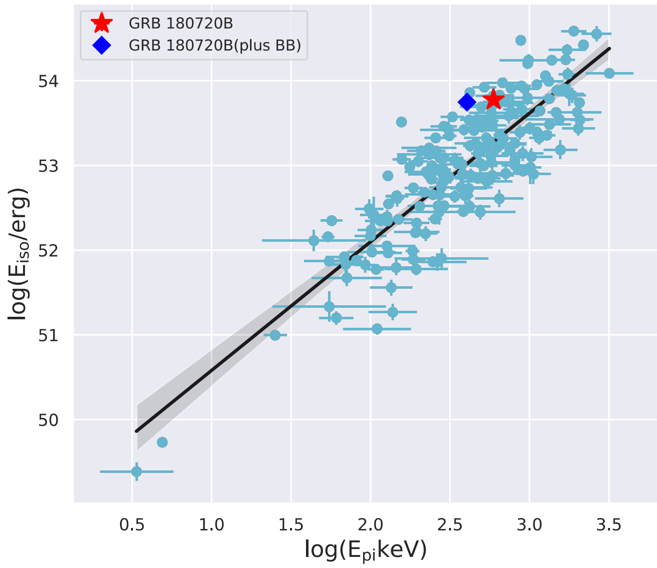

Figure 15. Amati relation of GRB 180720B. A flat Λ cold dark matter model with $\Omega_m = 0.3$ and $h = 0.7$ is assumed to convert S_{bolo} to E_{iso}. The blue points are samples from Huang et al. (2021). The blue diamond represents the Band model fitting alone, and the red five-pointed star represents the result of adding the BB fitting. The black line and shading are the best fit of the sample and the confidence interval of 0.95, respectively.

motivates us fit the spectra with a physics model. Finally, we used the synchrotron model to analyze the burst. It is found that the synchrotron model parameters p and B have a strong correlation with flux and show the time evolution behavior of double tracking. We compared the synchrotron model with the empirical model and found that the two model parameters have a strong correlation (α–p, log(B)–α, log(B)–log(E_p)).

We acknowledge the use of the public data from the Fermi data archives. This work is supported by the National Natural Science Foundation of China (grant 11763009, 11263006), Key Laboratory of Colleges and Universities in Yunnan Province for High-energy Astrophysics, the Natural Science Fund of the Liupanshui Normal College (LPSSY201401).

ORCID iDs

Zhao-Yang Peng https://orcid.org/0000-0003-3846-0988

References

Abdo, A. A., Ackermann, M., Ajello, M., et al. 2009, ApJL, 706, L138
Band, D., Matteson, J., Ford, L., et al. 1993, ApJ, 413, 281
Bhat, P. N., Fishman, G. J., Meegan, C. A., et al. 1994, ApJ, 426, 604
Borgonovo, L., & Ryde, F. 2001, ApJ, 548, 770
Briggs, M. S., Band, D. L., Kippen, R. M., et al. 1999, ApJ, 524, 82
Burgess, J. M. 2014, MNRAS, 445, 2589
Burgess, J. M., Bégué, D., Greiner, J., et al. 2020, NatAs, 4, 174
Burgess, J. M., Preece, R. D., Connaughton, V., et al. 2014, ApJ, 784, 17
Burgess, J. M., & Ryde, F. 2015, MNRAS, 447, 3087
Chhotray, A., & Lazzati, D. 2015, ApJ, 802, 132
Daigne, F., & Mochkovitch, R. 2002, MNRAS, 336, 1271
Deng, W., & Zhang, B. 2014, ApJ, 785, 112
Duan, M.-Y., & Wang, X.-G. 2019, ApJ, 884, 61
Firmani, C., Cabrera, J. I., Avila-Reese, V., et al. 2009, MNRAS, 393, 1209
Gao, H., & Zhang, B. 2015, ApJ, 801, 103
Ghirlanda, G., Ghisellini, G., & Lazzati, D. 2004, ApJ, 616, 331
Ghirlanda, G., Nava, L., & Ghisellini, G. 2010, A&A, 511, A43
Ghirlanda, G., Pescalli, A., & Ghisellini, G. 2013, MNRAS, 432, 3237
Golenetskii, S. V., Mazets, E. P., Aptekar, R. L., & Ilinskii, V. N. 1983, Natur, 306, 451
Granot, J., Komissarov, S. S., & Spitkovsky, A. 2011, MNRAS, 411, 1323
Gruber, D., Goldstein, A., Weller von Ahlefeld, V., et al. 2014, ApJS, 211, 12
Guiriec, S., Daigne, F., Hascoët, R., et al. 2013, ApJ, 770, 32
Hakkila, J., & Preece, R. D. 2011, ApJ, 740, 104
Huang, L., Huang, Z., Luo, X., He, X., & Fang, Y. 2021, PhRvD, 103, 123521
Iyyani, S., Ryde, F., Burgess, J. M., Pe'er, A., & Bégué, D. 2016, MNRAS, 456, 2157
Kaneko, Y., Preece, R. D., Briggs, M. S., et al. 2006, ApJS, 166, 298
Kargatis, V. E., Liang, E. P., Hurley, K. C., et al. 1994, ApJ, 422, 260
Kumar, P., & Zhang, B. 2015, PhR, 561, 1
Laros, J. G., Fenimore, E. E., Fikani, M. M., Klebesadel, R. W., & Kane, S. R. 1985, in ICRC, XIX Int. Cosmic Ray Conference, 4, (ICRC19), 5
Lazzati, D., & Begelman, M. C. 2009, ApJL, 700, L141
Lei, W.-H., Zhang, B., & Liang, E.-W. 2013, ApJ, 765, 125
Li, L. 2019a, ApJS, 245, 7
Li, L. 2019b, ApJS, 242, 16
Li, L. 2020, ApJ, 894, 100
Li, L., Geng, J.-J., Meng, Y.-Z., et al. 2019, ApJ, 884, 109
Liang, E., & Zhang, B. 2005, ApJ, 633, 611
Liang, E. W., & Dai, Z. G. 2004, ApJL, 608, L9
Lloyd, N. M., Petrosian, V., & Mallozzi, R. S. 2000, in AIP Conf. Ser. 526, Gamma-Ray Bursts, V Huntsville Symp., ed. R. M. Kippen, R. S. Mallozzi, & G. J. Fishman (Melville, NY: AIP), 145
Lu, R. J., Hou, S. J., & Liang, E.-W. 2010, ApJ, 720, 1146
Lu, R.-J., Wei, J.-J., Liang, E.-W., et al. 2012, ApJ, 756, 112
MacFadyen, A. I., & Woosley, S. E. 1999, ApJ, 524, 262
Meegan, C., Lichti, G., Bhat, P. N., et al. 2009, ApJ, 702, 791
Meng, Y.-Z., Geng, J.-J., Zhang, B.-B., et al. 2018, ApJ, 860, 72
Meszaros, P., & Rees, M. J. 1993, ApJ, 405, 278
Mészáros, P., & Rees, M. J. 2000, ApJL, 541, L5
Metzger, B. D., Giannios, D., & Horiuchi, S. 2011, MNRAS, 415, 2495
Moradi, R., Li, L., Rueda, J. A., et al. 2021, arXiv:2103.09158
Narayan, R., Paczynski, B., & Piran, T. 1992, ApJL, 395, L83
Norris, J. P., Share, G. H., Messina, D. C., et al. 1986, ApJ, 301, 213
Oganesyan, G., Nava, L., Ghirlanda, G., & Celotti, A. 2018, A&A, 616, A138
Oganesyan, G., Nava, L., Ghirlanda, G., Melandri, A., & Celotti, A. 2019, A&A, 628, A59
Pe'Er, A., Mészáros, P., & Rees, M. J. 2006, in AIP Conf. Ser. 836, Gamma-Ray Bursts in the Swift Era, ed. S. S. Holt, N. Gehrels, & J. A. Nousek (Melville, NY: AIP), 181
Pe'Er, A., Zhang, B.-B., Ryde, F., et al. 2012, MNRAS, 420, 468
Peng, Z. Y., Yin, Y., Bi, X. W., et al. 2010, ApJ, 718, 894
Preece, R. D., Briggs, M. S., Mallozzi, R. S., et al. 2000, ApJS, 126, 19
Rees, M. J., & Mészáros, P. 2005, ApJ, 628, 847
Ruffini, R., Siutsou, I. A., & Vereshchagin, G. V. 2013, ApJ, 772, 11
Ruffini, R., Siutsou, I. A., & Vereshchagin, G. V. 2014, NewA, 27, 30
Ryde, F. 2004, ApJ, 614, 827
Ryde, F., Axelsson, M., Zhang, B. B., et al. 2010, ApJL, 709, L172
Ryde, F., Pe'er, A., Nymark, T., et al. 2011, MNRAS, 415, 3693
Scargle, J. D., Norris, J. P., Jackson, B., & Chiang, J. 2013, ApJ, 764, 167
Siegel, M. H., Burrows, D. N., Deich, A., et al. 2018, GCN, 22975, 1
Uhm, Z. L., & Zhang, B. 2015, ApJ, 808, 33
Uhm, Z. L., & Zhang, B. 2016, ApJ, 825, 97
Uhm, Z. L., Zhang, B., & Racusin, J. 2018, ApJ, 869, 100
Vianello, G. 2018, ApJS, 236, 17
Vianello, G., Lauer, R. J., Younk, P., et al. 2015, arXiv:1507.08343
Vreeswijk, P. M., Kann, D. A., Heintz, K. E., et al. 2018, GCN, 22996, 1
Woosley, S. E., & Bloom, J. S. 2006, ARA&A, 44, 507
Woosley, S. E. 1993, in AIP Conf. Proc. 280, Proc. Second Compton Observatory Science Workshop, ed. M. Friedlander, N. Gehrels, & D. Macomb (Melville, NY: AIP), 995
Yu, H.-F., Hui, C. Y., Kong, A. K. H., & Takata, J. 2018, ApJ, 857, 120
Yu, H. F., Preece, R. D., Greiner, J., et al. 2016, A&A, 588, 135
Zhang, B. 2011, CRPhy, 12, 206
Zhang, B., & Mészáros, P. 2002, ApJ, 581, 1236
Zhang, B., & Pe'er, A. 2009, ApJL, 700, L65
Zhang, B.-B., Uhm, Z. L., Connaughton, V., Briggs, M. S., & Zhang, B. 2016, ApJ, 816, 72
Zhang, B. B., Zhang, B., Castro-Tirado, A. J., et al. 2018, NatAs, 2, 69
Zhang, B.-B., Zhang, B., Liang, E.-W., et al. 2011, ApJ, 730, 141